Article

Not peer-reviewed version

Characterizing Snow Dynamics in Semi-Arid Mountain Regions with Multitemporal Sentinel-1 Imagery: A Case Study in Sierra Nevada, Spain

Pedro Torralbo * , Rafael Pimentel , María José Polo , Claudia Notarnicola

Posted Date: 25 September 2023

doi: 10.20944/preprints202309.1582.v1

Keywords: Wet Snow; Sentinel-1; C-band; Synthetic Aperture Radar (SAR); Mediterranean Mountains; Semi-Arid Regions; Streamflow Dynamics

Article

Characterizing Snow Dynamics in Semi-Arid Mountain Regions with Multitemporal Sentinel-1 Imagery: A Case Study in Sierra Nevada, Spain

Pedro Torralbo [1,2]*, Rafael Pimentel [1,2], Maria José Polo [1,2] and Claudia Notarnicola [3,]

[1] Fluvial Dynamics and Hydrology Research Group, Andalusian Institute for Earth System Research, University of Córdoba, Campus Rabanales, Edificio Leonardo da Vinci, Área de Ingeniería Hidráulica, 14017, Córdoba, Spain; p12tomup@uco.es
[2] Department of Agronomy, Unit of Excellence María de Maeztu (DAUCO), University of Córdoba, Córdoba, Spain.
[3] Institute for Earth Observation, EURAC Research, Bolzano, Italy; claudia.notarnicola@eurac.edu
* Correspondence: Pedro Torralbo p12tomup@uco.es

Abstract: Monitoring snowmelt dynamics in mountains is crucial to understand water releases downstream. Sentinel-1 (S-1) synthetic aperture radar (SAR) has become one of the most widely used techniques to achieve this aim due to its high frequency of acquisitions and all-weather capability. This work aims to understand the possibilities of S-1 SAR imagery to capture snowmelt dynamics and related changes in streamflow response in semiarid mountains. The results proved that S-1 SAR imagery was able not only to capture the final spring melting but also all melting cycles that commonly appear throughout the year in these types of environments. The general change detection approach to identify wet snow was adapted for these regions using as reference the average S-1 SAR image from the previous summer, and a threshold of -3.00 dB. In addition, four different type of melting runoff onsets depending on physical snow condition were identified. When translating that at the catchment scale, distributed melting runoff onset maps were defined to better understand the spatiotemporal evolution of melting dynamics. Finally, a linear connection between melting dynamics and streamflow was found for long-lasting melting cycles, with a determination coefficient (R^2) ranging from 0.62 to 0.83 and an average delay between the melting onset and streamflow peak of about 21 days.

Keywords: wet snow; Sentinel-1; C-band; synthetic aperture radar (SAR); Mediterranean mountains; semi-arid regions; streamflow dynamics

1. Introduction

Mountains are considered "water towers" since they provide water for both ecosystems and anthropogenic demands in downstream areas [1-3]. In Mediterranean mountains, this role becomes more important since melting water from the snowpack can constitute the main water resource for human consumption, agriculture, and hydroelectric production [1]. The variability of the Mediterranean climate enhances the complexity of snow dynamics over these mountain regions [2]. The mild winter temperatures in combination with the long dry sunny period undergo in: (i) a highly variable snowpack, in time and space, with the presence of several accumulation and melting cycles during the snow season [3]; (ii) a shallow snowpacks with a characteristic patchy distribution [4]; (iii) a high snowpack density [5]; and (iv) a non-negligible evaposublimation flux from the snowpack to the atmosphere [6]. This peculiar snow dynamics conditions the seasonality of the streamflow response in the head-water catchments [2,5]. Therefore, it is key to deeply understand accumulation and melting dynamics of the snowpack to be able to foresee changes in downstream streamflow and consequently, in the water resources availability [7,8]

Physics of snow dynamics have been widely studied [9–11]. In a snowpack, during the accumulation phase snow water equivalent (SWE) increases, net energy inputs keep mainly negative and the average snowpack temperature decreases [12,13]. When these energy inputs become positive, due to external forcing, for instance radiation, snow turns into wet snow and the melting phase begins [14,15]. This melting period can be generally separated in three phases [11]: (i) moistening; (ii)

Preprints (www.preprints.org) | NOT PEER-REVIEWED | Posted: 25 September 2023 doi:10.20944/preprints202309.1582.v1

ripening ; and (iii) melting runoff. Traditionally, in-situ monitoring has been the principal tool used for observing and, therefore, understanding this snow dynamics [16]. However, the intrinsic limitations of accessibility, measurement representativeness and area coverage makes nowadays remote sensing one of the techniques extensively used for snow monitoring [10,11,17]. In addition, the possibility to use free satellite imagery on cloud platforms such as Google Earth Engine (GEE) is also expanding their use [26–28]. Optical sensors, not just satellite sensor but also terrestrial photography, have been exploited to derive snow cover maps [8,13,18,19] and to compute snow albedo [20–22], while, microwave information has been used to retrieve SWE from the snowpack [23–25] , to estimate snow depth [29], and to differentiate between dry and wet snow [12,25,26].

In this last case, this differentiation is based on the fact that the presence of water in the snow cover generates high dielectric losses that provoke significant reduction in radar backscatter [27]. This drop in the signal has been recently demonstrated that is considerably visible and sensible in the cross-polarization VH [28,29]. In particular, the new Sentinel-1 (S-1) SAR constellation, which has a dual polarization capability, very short revisit times, high spatial resolution, rapid product delivery and open access to all imagery [30], has become widely used in different applications that use wet-snow information [22–25]. For instance, in [31], the author used S-1 for characterizing wet snow to quantify mass balance over Greenland. In the same path, snowmelt over the ice sheets in Antarctica were characterized [32]. In [33], the authors used wet-snow identification for characterizing ice avalanches while in [28], they have successfully characterized snowmelt phases using SAR in an Alpine environment. Moreover, in [20], it is concluded that minimum SAR backscattering is reached at the end of the ripening phase and at the beginning of the melting-runoff phase. At that moment all liquid water content is held in the snowpack and starts to be released. From this onset, a monotonic increase in the backscattering is found until the snowpack is melted. Over these environments, snowpack is well consolidated during the winter, has thick depths and generally a unique snowmelt cycle during the springtime. Mediterranean mountains, located in semi-arid regions, are unlikely to have just one accumulation-melting cycle and suffer such slow transitions [2,4,5,34]. Indeed, in these areas the main characteristics are generally quicker snowpack changes, several melting cycles throughout the year and perhaps with the loss of some of the three defined melting phases due to this quick response [3,35].

From a hydrological point of view, the melting runoff onset provides the moment when melting water goes out of the snowpack and starts to contribute as liquid water into the system. Finding a relation between this onset and the streamflow response can help forecast streamflow behavior due to runoff melting [36,37]. In fact, the actual warming situation is altering this timing and increasing the need of a correct representation of this onset [38,39]. However, the paths followed by runoff melting water for reaching the stream are multiple and difficult to differentiate [40]. In general, runoff melting water after leaving the snowpack arrives at the upper part of the soil [41]. From there, meltwater infiltrates into the soil and/or accumulates to form a saturated zone at the base of the snowpack, moving toward a surface-water body following different paths that are conditioned by soil characteristics[42]. If soil is unsaturated and water table is low, the water infiltrates and moves stream ward as subsurface flow. On the contrary, if soil is close to the saturation state, meltwater accumulates to form a basal saturated zone that develops within the snowpack through which water flows toward the stream [11]. One can therefore conclude that melting dynamics are directly linked to baseflow response of the catchment.

In this context, the main objective of this study is twofold, first to explore the capability of C-band S-1 SAR imagery to capture multi seasonal wet snow dynamics over Mediterranean mountain areas and second, to apply a hydrological approach to assess the connection between this wet snow dynamics and streamflow response. In this work the main innovative parts are: i) the jointly use of terrestrial imagery and satellite information to deeply understand S-1 SAR backscattering response at the local scale; ii) the use of S-1 SAR imagery to characterize snow melting not only during the spring melting but throughout the hydrological year; and iii) the applicability of S-1 SAR imagery to identify runoff melting onset and to relate this behavior to changes in the streamflow dynamics at

Preprints (www.preprints.org) | NOT PEER-REVIEWED | Posted: 25 September 2023 doi:10.20944/preprints202309.1582.v1

the catchment scale. The Sierra Nevada Mountain Range (southern Spain) is selected as pilot Mediterranean mountain area to carry out this study.

The paper is structured into five sections. Section 2 presents the test sites at a local and catchment scales. It also includes the meteorological data available as well as the remote sensing information used. In section 3, we present the different steps of the proposed approach to detect wet snow conditions and the definition of melting cycles. The results are exposed in Section 4, focusing on the local and catchment scale. In section 5, we discuss the main results. Finally, section 6 draws the conclusions of the work, by providing information on how the proposed methodology can be extended to other semi-arid mountains.

2. Study site and available data

2.1. The Sierra Nevada Mountain Range

The Sierra Nevada Mountain Range (southern Spain, Figure 1(a)) is the southernmost mountain range in Europe, with elevations that go up to 3479 m a.s.l. and it is only overcome by the European Alps. It covers approximately 80 km long in the East–West direction and 27 km wide in the North–South direction (Figure 1 (b)). Alpine and Mediterranean climates coexist in the range. The alpine climate of high altitudes is modified by the proximity to the seacoast together with an abrupt topography, high radiation rates, and low relative humidity. The precipitation regime is highly variable, with annual precipitation values that can vary from dry years, with 200 mm of total precipitation, to wet years, with almost 1000 mm [2]. Regarding temperature, the annual mean daily temperature in the area is about 12.6 ºC, being minimum daily temperatures no longer negative from April to November [43]. Snow in the range frequently appears above 2000 m a.s.l. between October and May. Mediterranean boundary conditions deeply affect snow characteristics, remarkably in the southern face of the range. Among these characteristics, the shallow and high density snowpacks [44], the high evaposublimation rates [6] and the appearance of more than one accumulation-melting cycles during the snow season [3] are the ones that stand out the most. Streamflow in the downstream catchments is highly conditioned by this snow dynamics. Streamflow usually has several peaks linked to each one of the accumulation-melting cycles.

Low creeping vegetation and shrubs are the main vegetation in the area, particularly in upper altitudes. The *Hormathophylla spinosa*, the *Genista versicolor* and the *Festuca clementei* are the most common shrub types in the mountain range. Forestry high vegetation such as pine trees are not very common, only in some reforested isolated pieces of land. All these physical and specific characteristics make Sierra Nevada one of the most important centers of biodiversity in the Mediterranean regions. Thus, this region was declared UNESCO Biosphere Reserve in 1986, Natural Park in 1989 and National Park in 1999.

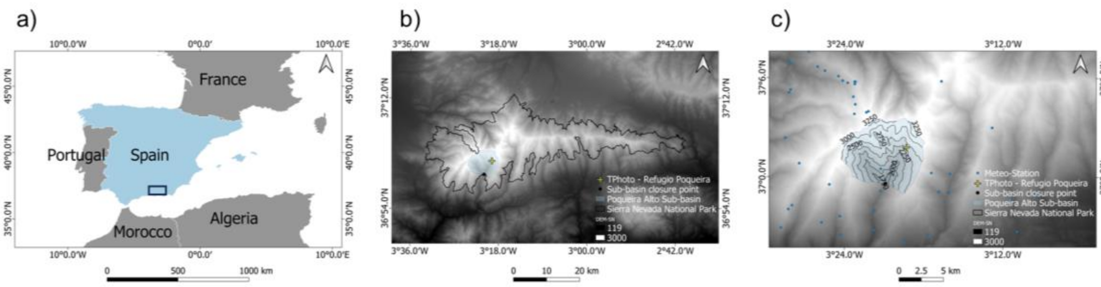

Figure 1. Location of Sierra Nevada within Spain; (b) Relief of the Sierra Nevada Mountain range with the location of the two study sites: Refugio Poqueira (yellow cross) and Poqueira Alto Catchment (blue polygon); (c) Zoom of the target areas.

Within Sierra Nevada Mountain range, this study was carried out at two different scales by using two study sites:

- Plot scale - The Refugio Poqueira experimental site (Figure 1 (c), yellow cross). This area was selected to understand the connection between backscatter signal and snow dynamics. It is

Preprints (www.preprints.org) | NOT PEER-REVIEWED | Posted: 25 September 2023 doi:10.20944/preprints202309.1582.v1

located at 2500 m a.s.l. and has been highly monitored since 2004 focusing on the microscale effects on snow ablation in Mediterranean mountains. The experimental site is equipped with a complete weather station (Table 1).

- Catchment scale - The Poqueira Alto catchment (Figure 1, (c)). This catchment was selected as a study site to connect wet snow dynamics with streamflow response. It is a small catchment (54.91 km^2) corresponding to the headwaters of the Poqueira River. With a mean elevation of 2513 m a.s.l., its hydrological response is totally driven by the snow dynamics (Table 1).

2.2. Available Data

This study was carried out for four hydrological years, from 2016-2017 to 2019-2020. The three first years were used to understand wet snow dynamics and its connection to streamflow. The last year was used as an evaluation year to test our findings. Three data sources have been used in this study: meteorological information, remote sensing imagery and streamflow simulations.

2.2.1. Meteorological information

Records from the Refugio Poqueria weather station (PG2,[45]) were used in the study at the plot scale. This weather station is equipped with different sensors that generate 5-minute data records pertaining to precipitation, solar radiation, long-wave radiation, wind velocity, temperature, air humidity, and atmospheric pressure. Data aggregated at daily scale were used in this study.

At the catchment scale, meteorological daily information from the three nearest weather stations (Figure 1, small blue dots) has been interpolated by spatial algorithms that consider topographic effects and aggregated at the catchment scale. Specific spatial interpolation algorithms for each of the available variables were used [46]. Precipitation-elevation linear gradients have been locally defined for each variable (i.e., precipitation, temperature, and radiation) by using historical datasets and a least square error method. Thereafter, the residuals were calculated by using linear gradients. The square inverse distance weighting (IDW2) was used for interpolation by using the three closest stations and added to the theoretical value calculated using the linear gradient [46–48]. This data has been used for computing average meteorological information at the catchment scale.

Table 1. Summary of the selected characteristics of each region (see Figure 1) in the study area (SN), together with climate variables during the reference period 2016–2019.

Variable	Refugio Poqueira (A1)	Poqueira Alto (A2)
Area	30x30 (m^2)	54.9 (km^2)
Average altitude (m a.s.l.)	2500	2513
T mean (ºC) (max / mean / min)	21.8 / 6.95 / -9.55	12.89 / 7.018 / 0.91
Tdaily max (ºC) (max / mean / min)	24.522 / 9.375 / -6.36	17.61 / 10.54 / 3.86
Tdaily min (ºC) (max / mean / min)	19.287 / 4.34/ -11.46	8.697 / 4.03 / 0.00
Precipitation (mm)	2016-2017: 704 2017-2018: 745 2018-2019: 587	2016-2017: 785 2017-2018: 937 2018-2019: 690
Snowfall (mm)	2016-2017: 394 2017-2018: 384 2018-2019: 244	2016-2017: 438 2017-2018: 544 2018-2019: 358

2.2.2. Proximal and remote sensing observations

Terrestrial photography

Terrestrial photography from a camera, CC640 Campbell Scientific, installed at the Refugio Poqueira weather station was used in the study at the plot scale to improve the understanding wet

Preprints (www.preprints.org) | NOT PEER-REVIEWED | Posted: 25 September 2023 doi:10.20944/preprints202309.1582.v1

snow dynamics. The images acquired by the camera cover an area of about 30 x 30 m (equivalent to the spatial resolution of the Landsat TM sensors). The camera acquires 5 pictures a day, every 2 hours from 8:00 AM to 16:00 PM, with a resolution of 640 x 504 pixels. Following the methodology proposed by [3], snow cover area (SCA) times series were derived and used in this study. Automatic inspection was carried out to remove those images of bad quality due, for instance, to cloud cover, fog, or rain.

Sentinel-1 SAR imagery

The S-1 two satellite constellation was used in this study. They can collect C-band SAR imagery with different polarizations and pixel resolutions with a revisit time of 6 days. This has not affected this work as the analyses were carried out until 2020. In our analysis, the interferometric wide swath mode was used with a 3.5 x 22 m resolution. The orbits covering the Sierra Nevada mountains are the 1 and 81, in afternoon and in the morning respectively. The signal has a local incidence angle range around 35° (afternoon) and 36° (morning), that is, it is within the threshold where backscatter and theory show lower separability of the two classes for co-polarized backscatter (VV and VH) at low local incidence angles [49,50]. This study has focused on the afternoon images as it offers a clearer identification of the snowmelt phases while the morning acquisitions can be affected by melt-freeze component. The local acquisition time is approximately the 18:10 GMT+1. In total, 30 scenes in the 2016-2017 period, 51 scenes in the 2017-2018, 42 scenes in the 2018-2019 period and 49 scenes for the last year were processed and analyzed.

Optical MODIS data: MOD10A2 product

MOD10A2 version 006 product was used to assess snow dynamics at the catchment scale. This product has an 8-day composite and 500 x 500 m spatial resolution. This MODIS product was selected because it offers the possibility to have long and consistent time series, as well as a temporal resolution of 8 days, close to the 6 days of S1-SAR. A total of 156 scenes were employed in the study period from 2016 to 2019.

2.2.3. Streamflow data

Simulated streamflow data from WiMMed (Watershed Integrated Model for Mediterranean Environments were used [48]. WiMMed distributed physically based model is composed of several modules. Among them, the snow module (SnowMed) uses a punctual mass and energy balance extended to a distributed scale using depletion curves [3]. Actual evapotranspiration is calculated using the Penman-Monteith PE formulation [51,52] whereas infiltration is estimated using the Green and Ampt [53] approach in a two-layer soil discretization. Groundwater is modeled as two serial linear buckets, which represent quick and low groundwater response [54]. The model was developed specifically for Mediterranean environments and was calibrated and validated in the area of Sierra Nevada (Pearson correlation coefficient of 0.84, Kling Gupta Efficiency (KGE) of daily streamflow values of 0.59, and mean absolute bias in the daily river discharge of 1.9 m^3/s [55]. WiMMed simulates the different streamflow components. In this study we used baseflow due to its connection to the melting dynamics. In addition, snow simulations were used to characterize SWE values over certain targeted periods.

3. Methodology

The methodology used is composed of two main parts: (i) Definition of snowpack wet snow dynamics and (ii) assessment of hydrological implication of wet snow dynamics. The identification of melting cycles was used as a first step to determine the periods of time when snow can significantly impact streamflow. The overall flow of the procedure is illustrated in Figure 2.

 doi:10.20944/preprints202309.1582.v1

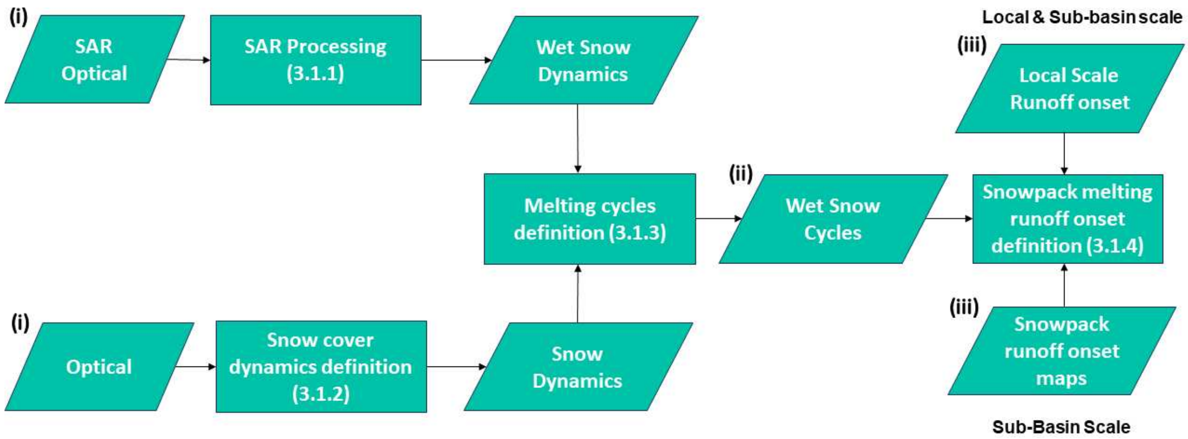

Figure 2. Workflow of the proposed approach where the main sections are identified in brackets. The inputs are SAR and MODIS images for section (i), the cycles are the results of the first step that is then used as an input to be interpreted at a local scale (ii) and at a sub-basin scale (iii).

3.1. Definition of snowpack wet snow dynamics

A preprocessing of SAR and optical imagery was carried out to define wet snow (section 3.1.1) and snow cover (section 3.1.2) dynamics, respectively. Both inputs were combined to identify snow melting cycles (section 3.1.3). Once melting cycles were defined runoff melting onset definition was performed (section 3.1.4). The snowpack runoff melting onset was calculated at two scales: (i) plot scale, for runoff melting onset understanding and (ii) catchment scale, for runoff melting onset maps definition (Figure 2).

3.1.1. SAR Processing

In this study, we followed the change detection approach by Nagler and Rott [56–58] to differentiate wet snow phases within the snowpack. The SAR intensity signal depends on these parameters: i) the sensor characteristics; ii) the snowpack properties; and iii) the ground properties. The interaction of the SAR signal with the snowpack are determined by the presence of water particles in the snowpack. As moisture increases, the SAR backscattering reduces in intensity since part of it is absorbed by the water particles [28,57,59]. The followed approach foresees the use of two images i) a reference image acquired during snow-free or dry conditions [57,58,60–62]; and, ii) a image of the period of interest, such as the melting season. The difference of the two images allows the detection of main changes such as those related to wet snow presence and reduces the influence of other factors such as the topography. In this direction, the two images need to be acquired with the same geometry [63]. The methodology can be described in three main steps: (i) SAR image preprocessing; (ii) Reference image selection; and (iii) Wet snow threshold definition.

SAR image preprocessing

The time serial S-1 SAR images were processed to obtain the operable ortho-corrected product with a pixel size about 10 x 10 m [64]. We use the GEE platform, which included the S-1 Toolbox to preprocess the "COPERNICUS/S1 GRD" collection. In particular, the Interferometric Wide Swath (IW) with polarization VH was chosen. The cross-polarization VH was selected because is highly sensitivity to changes in water content and therefore, sensitive to wet snow within in the snowpack [28,29,65]. The pre-processing applied in GEE consists of i) GRD border noise removal, ii) Thermal noise removal, iii) radiometric calibration and iv) terrain correction. Moreover, a threshold filter of -25 dB was applied to consider the noise floor of the sensors [66,67]. Additionally, areas in layover and shadow considering the local incidence angle (LIA) for each pixel were masked [68]. SAR images were resampled to 30 x 30 m using areal interpolation. This resolution was considered optimal for

Preprints (www.preprints.org) | NOT PEER-REVIEWED | Posted: 25 September 2023 doi:10.20944/preprints202309.1582.v1

snow studies over this area [3]. In addition, this spatial resolution contributes to reduce the speckle noise in S-1 SAR imagery. MOD10A2 version 006 product is used to discriminate snow cover extension. This product provides information on the snow cover extent based on the NDSI (Normalized Difference Snow Index) value with a 500 x 500 m ground resolution. A pixel is considered as snow pixel if its NDSI value is above 0 [19,69,70]. Snow cover extension maps were also resampled at 30 x 30 m using, in this case, a nearest neighbor interpolation algorithm.

Reference image selection

The derivation of wet snow pixels in a certain area was based on a change detection approach by comparing the image under analysis with a reference image [57], which was acquired with the same geometry on a date where the areas were supposed to be covered by dry snow or non-snow. This approach has the advantage to remove common features of the images such as topography that can influence the backscatter signal. Therefore, the first step was the definition of this reference image. Different studies such as [56–58,71,72] used either an image with snow dry conditions, for instance a imagery from January, or a snow free image, such as July or August. This is due to the fact that the backscattering in both cases is similar as dry snow is transparent for C-band signal [73–75]. Therefore, it was important to objectively define our period of reference. A sensitivity analysis was carried out to identify the best period for the reference images [76]. Indeed, the characteristics of the snow in this Mediterranean area, with several accumulation-ablation cycles throughout the year and in general a quick melting processes, makes it difficult to select a dry snow winter image. Therefore, we selected several summer images in four combinations: 1) the average value of all the summer months of the subsequent year, 2) the average value of only the images that have 15 previous days without rain of all the summer months of the subsequent year, 3) the average value of all the summer months of the previous year and 4) the average value of only the images that have 15 previous days without rain of all the summer months of the previous year.

The results of the sensitivity analysis indicated that no big differences were found between the four options tested when selecting reference imagery (Figure A1, see Appendix A). When analyzing them in pairs, the average difference was 0.34 dB ranging from 0.33 to 0.36 dB. Finally, we decided to select the average value of the previous summer as reference dataset. Two were the reasons: its calculation simplicity and the fact that this constitutes an antecedent information to the analyzed snow season and therefore can be used in near-real time applications.

Wet snow threshold definition

Once the difference image ($\Delta\sigma$) is derived, a threshold to identify wet snow conditions needs to be fixed. This wet snow threshold was obtained by evaluating the two distributions of wet-snow and dry/non-snow pixel values and identifying where they overlapped [57,72,77]. This overlapping defines the minimum threshold value to identify whether a pixel is dry or wet.

In our case more than 2500 pixels of the area of Sierra Nevada were chosen as regions of interest and their statistics were calculated to finally obtain this threshold value. Different dates were chosen from several years. This allowed us to consider more than one type of snow conditions and more than one season, being the results more robust. The selected scenes correspond to the following dates i) 2016-12-05, ii) 2017-03-05, iii) 2018-02-16, iv) 2018-02-28, v) 2019-04-12 and vi) 2019-04-24. Threshold values varied from -2.20 dB to -3.88 dB for the different selected images, as can be seen in Figure A2 (see Appendix). Average values indicate a threshold value of -2.83 dB. Based on this result and for simplicity reason, we have used a – 3.00 dB threshold.

3.1.2. Snow cover dynamics definition

Accumulation and melting phases of snow cycles throughout the study period were defined at the two different study scales. At the local scale, terrestrial photography was used to characterize these cycles. In addition to the fractional snow cover (FSC), these images were used to evaluate whether it was snowing, melting or no-changes occurred in the snowpack. Increasing and decreasing

 doi:10.20944/preprints202309.1582.v1

stages defined accumulation and melting phases respectively. MOD10A2 version 006 products were used to characterize snow dynamics at the catchment scale.

3.1.3. Melting cycles definition

A snow melting cycle generally has three phases: (i) moistening, (ii) ripening and (iii) melting runoff [11]. First, in the moistening phase, in which average snowpack temperature increases until the snowpack is isothermal, the snowpack is accumulating energy in the form of latent heat for being able to start melting. Second, in the ripening phase, actual melting begins but the meltwater is retained in the snowpack. That is, liquid water content of the snowpack increases but water does not go out of the snowpack. Third, in the melting runoff phase further energy inputs produce a water output from the snowpack. From that time onwards, water follows its path until reaching the streamflow.

Wet snow conditions can be detected by using SAR imagery and therefore relate these states with melting phases in the snowpack. For that, over the $\Delta\sigma$ signal, we defined a pixel as wet snow pixel if it has a value lower than -3.00 dB (see section 3.1.1). In each melting cycle we defined Local Minima (LMs) of the $\Delta\sigma$ time series as possible melting runoff onsets [28]. More than one LMs can be identified in the same melting cycle depending on the aging process of the snowpack (i.e., snowpack refreezing, rain on snow events).

At catchment scale, individual pixels' LMs were aggregated. That is, for each date, the total number of pixels with LMs in the catchment were calculated (ΣLM). This ΣLM time series define potential area of the catchment contributing to the melting runoff in each date. Larger number of ΣLM implies larger snow contributing areas to the melting runoff. The melting cycles were defined combining the ΣLM time series with the FSC time series (see section 3.1.2). A melting cycle was defined if there was an increase in the number of pixels with ΣLM and FSC was maintained or decreased (Figure 3). That is, the existence of large amounts of minima during a date with significant loss of snow area confirm the possible contributions of water to the system. Then, for each melting cycle the absolute LM within the melting cycle was identified. This LM will provide the actual melting runoff onset for each pixel in this cycle, that is a Local Minima onset (LMo).

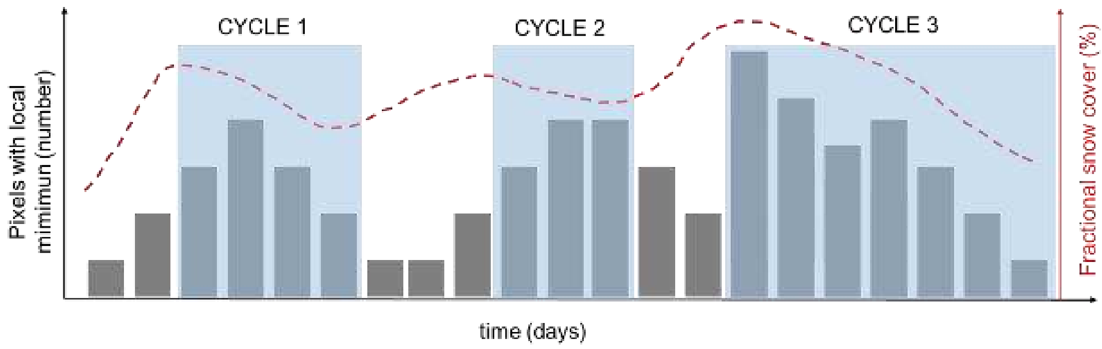

Figure 1. Scheme of melting cycle definition

3.1.4. Identification of the relationship between snowpack melting and runoff onset

Local Scale Runoff onset interpretation

At the local scale, we identified the onset of melting runoff when LM takes place. We used this scale to understand the relation between the backscattering signal, the presence of wet snow pixels and the snow dynamics. For that, we used the meteorological information of the Refugio Poqueira weather station and the terrestrial photography of the area. In this process these images were used not only to define snow dynamics, but also, to better understanding snow processes. That is, they helped relating changes in the snowpack to changes in backscattering signals; for instance, the identification of rapid snow melting between two consecutive SAR images, the occurrence of rain on snow events, and the changing in snow surface roughness.

Snowpack runoff onset maps

At the catchment scale, for each pixel of the catchment and for each one of the identified cycles, we defined the LMo. This date will mark the onset of the melting runoff of this pixel [28]. At catchment scale, we ended up with a distributed map that provides the beginning of the melting runoff, LMo, for each pixel in the whole catchment. To understand the distribution of those dates over the catchment in each cycle, a combined analysis in relation to catchment features (e.g., elevation) and variables affecting the beginning of the melting runoff (e.g., radiation, temperature) was conducted.

3.2. Wet snow - streamflow interaction

We analyzed the relationship between wet snow presence and streamflow dynamics with aim to assess the potential of S-1 SAR imagery to foresee changes in streamflow. For that we used the concept of depletion curve highly used in hydrology; for instance, to study the evolution of snow cover [3] and its relationship with streamflow [78–80] or its relationship with SWE [81]. To build these curves we used two variables: (1) the cumulative number of pixels contributing to melting runoff in each cycle (ΣLMo), which represent wet snow dynamics; and (2) the cumulative baseflow, which represent streamflow dynamics. Baseflow is used since it is the component of the streamflow that is more influenced by the melting dynamics. To make the depletion curve between cycles comparable we dimensionless the target variables by their maximum value in each of the analyzed melting cycles.

4. Results

4.1. Definition of snowpack wet snow dynamics

4.1.1. Local Scale: Backscatter signal understanding

At the local scale, the connection between SAR backscattering signal and snow dynamics was explored during the three hydrological years: 2016-2017, 2017-2018 and 2018-2019. Meteorological information and terrestrial photography at the Refugio Poqueira weather station were used in this process. Annual snowfall values varied between years, with 394 mm, 384 mm, and 244 mm respectively. Temperature patterns also changed during years, with annual mean daily values of 7.5 ºC, 6.1 ºC, and 7.4 ºC, for each hydrological year in the study period respectively (Figure 4a, b and c, upper panel). This variability implies that the number of snow cycles also varies in each of the analyzed years. These snow dynamics were defined combining terrestrial photography (changes in the snowpack) and meteorological information (snowmelt events) on a daily scale at the target area (see section 3.1.2.). Fig 4 shows lines in the top and bottom of each gray rectangle identifying an accumulation (blue) or melting (red) phase of each of this snow cycle (Figure 4, gray rectangles).

In 2016-2017 (Figure 4, a) six LMs were identified, four in the first melting cycle, one in the second cycle and another one in the third. LM1 (-4.00 dB) was found in the third week of November corresponding to the beginning of the snow season. At this stage, the energy exchange between the snowpack and the ground increased the liquid water content of the snowpack, reaching this local minimum in the $\Delta\sigma$ signal. Water content highly increased in LM2 (-9.50 dB), 5th December, with the lower $\Delta\sigma$ value of the year. This LM was preceded by a significant snowfall period, which was followed by a rain on snow event and an increment of the temperature that increased the water content again. A coolest period occured after that, which made the snowpack to dry out. A significant increase in temperatures provoked LM3 (-3.50 dB) the second week of December. Again, a cool period stabilized the signal until the combination of precipitation and increasing temperatures generated LM4 (-6.00 dB), the 21st of February, which can be defined as the onset of spring melting runoff. LM5 (-4.00 dB) and LM6 (-5.00 dB) corresponded to faster melting cycles, whose shallow snowpack provoked a quick melting due to the energy exchanges between the snowpack and the ground.

For the second analyzed year, 2017-2018 (Figure 4, b) four LMs were identified, one in the first melting cycle, one in the second cycle and two on in the third one. The first local minimum LM1 (-5.00 dB) was found in mid-December and corresponded to a shallow snowpack that quickly melted

Preprints (www.preprints.org) | NOT PEER-REVIEWED | Posted: 25 September 2023 doi:10.20944/preprints202309.1582.v1

after a light snowfall. For the second melting cycle, liquid water content increases in LM2 (-4.50 dB) corresponding to an increase of the temperatures. However, the melting did not continue since the temperature dropped again. The Δσ signal was not able to capture the onset of the melting runoff of this cycle since it occurred in the period between images. For the last cycle of this year, wet snow was present since the beginning of the cycle due to higher temperatures during this period. Two LMs were found, while the melting onset started on the 5th of April, with LM3 (-12.00 dB), in which the snowpack was cooled by a snowfall event that made the appearance of another local minimum LM4 (-10.00 dB) that finally triggered the spring melting.

The third analyzed year, 2018-2019 (Figure 4, c), was the driest of the analyzed ones. Seven short melting cycles were identified. One LM is defined in each of them. All LMs follow the same dynamics, quick melting after a light snowfall. The first cycle was so quick that the Δσ signal was not able to capture the presence of wet snow. That is LM1 was above the wet-snow threshold of -3.00 dB. The Δσ signal reached values of -3.50 dB for LM2 and -8.00 dB for LM3, the Δσ rapidly recovered its values by the time the snow cover disappeared. Then, between late January and February, two LMs were identified, LM4 (-4.00 dB) and LM5 (-6.00 dB). LM6 (-6.00 dB) can be identified as an actual spring melting runoff onset since the length of this melting cycle is the longest and the accumulated snow was the highest of the year. Finally, the last LM occurred during April LM7 (-6.00 dB) triggered again by an energy exchange between the snowpack and the ground demonstrated by higher temperatures that heated the ground.

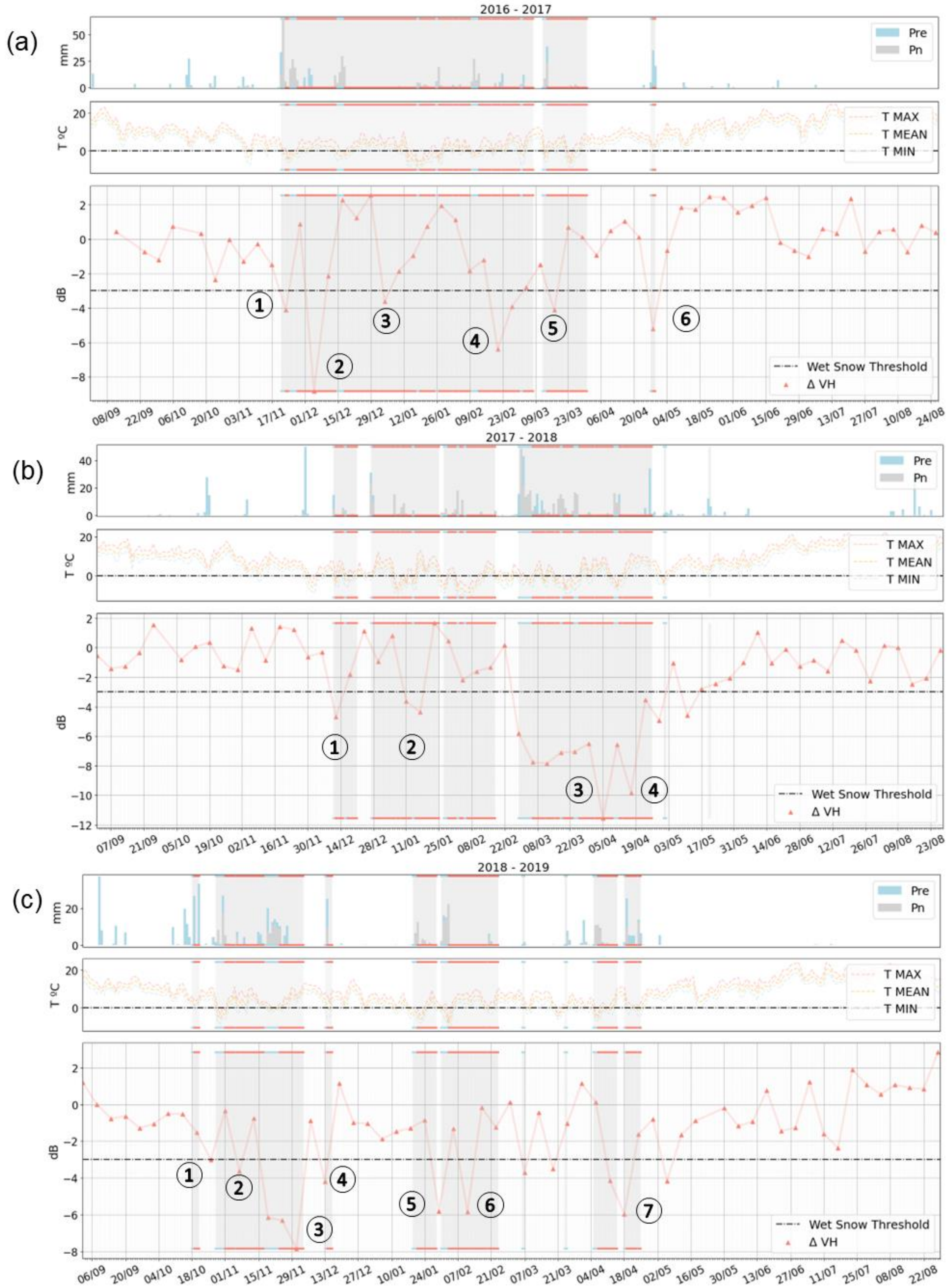

Figure 4. Temporal evolution of analyzed variables for three hydrological years: (a) 2016-2017, (b) 2017-2018, (c) 2018-2019. For each year: (i) the upper panel shows precipitation (blue bars) and snowfalls (gray bars) evolution; (ii) the intermediate panel represents the temporal evolution of daily temperatures, maximum (red), mean (orange) and minimum (blue); (iii) the bottom panel shows the evolution of the difference backscattering between the reference image and the day of interest. (red line with triangles). The dashed line in the bottom panel marks the wet snow threshold defined for the study area. In all panels, the presence of snow in the study area is highlighted by using a gray rectangle; lines in the top and bottom of this rectangle identify an accumulation (blue) or melting (red) phase.

Preprints (www.preprints.org) | NOT PEER-REVIEWED | Posted: 25 September 2023 doi:10.20944/preprints202309.1582.v1

Local Minima Classification

The previous analysis of Δσ signals evolution at the local scale and the identification of different LMs allowed to explain their evolution in relation to snowpack dynamics over these areas. Starting with the hypothesis that a LM triggers the onset of melting runoff and the four types of melting cycles identified by [3] for the study area, four types of LMs in the Δσ signal were identified (Table 2) (Figure 5).

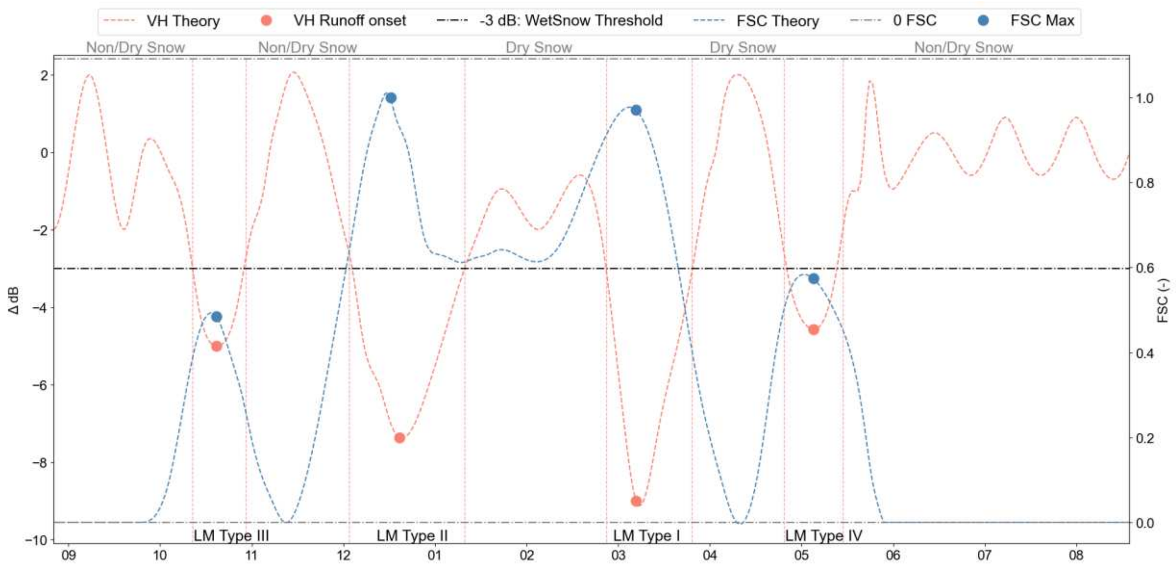

Figure 5. Definition of four types of local minima (red dots) identified for Mediterranean mountain area. VH represents the theoretical distribution of the Δ dB of S-1 SAR backscattering of the cross-polarization VH. FSC represents the temporal distribution of snow cover fraction. Blue dots represent the maximum snow cover fraction. Periods without snow or with dry snow are also specified on the upper axis. The x axis represents the temporal variation over a hydrological year (Sep-Aug) of the different variables, the y axis represents the corresponding value of the Δ dB of S-1 SAR backscattering (left y axis) and snow cover fraction (right y axis).

- Local Minimum Type I: the LM is found at the end of a well-developed snowpack. It is representative of long-lasting snow cycles, with a large amount of snow, resulting from a long accumulation phase, and it is associated with a very compact state of the snow with a high level of metamorphism. This LM is found in melting cycles described by depletion curve Type I in [3].
- Local Minimum Type II: the LM is not unique in the snow cycle. It describes a quick melting period that is stopped by another snowfall or cold period that refreezes snow. This LM is found in melting cycles described by depletion curve Type II in [3].
- Local Minimum Type III: the LM is unique withing the melting cycle, that is before and after this LM there is no snow. In addition, it takes place at the beginning of the snow season, when the energy exchange between the snowpack and the ground causes LWC to increase. This LM is found in melting cycles described by depletion curve Type III in [3].
- Local Minimum Type IV: as in the previous case the LM is unique, that is before and after this LM there is no snow. However, in this case the minimum appears in sporadic snow cycles that occur during late winter or spring, always after the main melting cycle. The LM is connected to a melting trigger by an increase in the temperature and incoming flux of shortwave radiation. This LM is found in melting cycles described by depletion curve IV in [3].

Table 2. Local scale classification of LMs based on the four LM types explained in Figure 5.

Type I	Type II	Type III	Type IV
LM4 2016-2017	LM1, LM2, LM3, LM5, 2016-2017	LM1 2017-2018	LM6 2016-2017

Preprints (www.preprints.org) | NOT PEER-REVIEWED | Posted: 25 September 2023 doi:10.20944/preprints202309.1582.v1

LM4 2017-2018	LM2, LM3 2017-2018	LM1, LM4 2018-2019	LM7 2018-2019
LM3, LM6 2018-2019	LM2, LM6 2018-2019		

4.1.2. Catchment Scale: Melting Runoff Onset Maps

The plot scale results were extrapolated at the catchment scale. The individual analysis carried out for a single pixel was performed in each of the pixels of the selected catchment for the three hydrological years analyzed (Figure 6, 7 and 8, a) and b). First, melting cycles were identified following the methodology proposed in section 2.1.3. Three melting cycles were defined for the two first hydrological years, while four melting cycles were defined in the third hydrological year analyzed (Table 3). The duration of these cycles varied within the year (Table 3). While for the year 2016-2017 and 2017-2018, a long-lasting spring melting cycle was identified (C-3 in each year), in the case of last year, 2018-2019, two were the melting cycle with longer duration (C-3 and C-4). Each of these cycles was associated with an increasing event of baseflow in the outlet of the catchment, which was delayed a certain number of days depending on the cycle (Figure 6, 7 and 8, c). Deeper connection between streamflow and melting cycle is analyzed in section 4.2.

Table 3. Summary of the characteristics (beginning date, end date, cumulative precipitation, and cumulative snowfall) of snowmelt-accumulation events identified in each of the hydrological year analyzed.

Melting Cycle	Beginning	End	Duration (days)	Precipitation (mm)	Snowfall (mm)	Average daily Temperature (ºC)	Average minimum daily Temperature (ºC)	Mean SWE (mm)	Maximum SWE (mm)
					2016- 2017				
C-1	17-11-2016	05-12-2016	18	256	159	0.5	-3.0	85.2	140.2
C-2	11-12-2016	04-01-2017	24	92	67	1.3	-2.0	85.8	125.2
C-3	09-02-2017	04-05-2017	84	233	140	3.5	-0.6	23.9	78.7
					2017- 2018				
C-1	05-01-2018	23-01-2018	18	41	36	0.2	-4.0	14.3	26.4
C-2	29-01-2018	16-02-2018	18	32	31	2.9	-7.2	12.43	25.9

Preprints (www.preprints.org) | NOT PEER-REVIEWED | Posted: 25 September 2023 doi:10.20944/preprints202309.1582.v1

C-3	28-02-2018	09-08-2018	162	585	395	7.3	3.2	43.3	184.5
					2018 – 2019				
C-1	26-10-2018	07-11-2018	12	70	47	0.9	-3.5	14.4	34.5
C-2	13-11-2018	12-01-2019	60	139	85	3.7	0.4	13.8	52.3
C-3	30-01-2019	19-03-2019	48	85	72	2.5	-1.4	10.7	61.4
C-4	31-03-2019	23-06-2019	120	171	104	7	2.8	5.5	43.4

For each of these cycles, the LMo in each pixel was identified as the melting runoff onset over the catchment to produce individual maps of LMo distribution (Figures 6, 7 and 8, bottom panels).

The first cycle of the year 2016-2017 (Figure 6 C-1) showed that pixels located in low elevation reached first the LMo. These LMo were identified a LM Type III, that is, they corresponded to shallow snowpack where melting takes place due to an energy exchange between the snowpack and the ground. Pixels at high elevation were distributed without a clear pattern along the other three dates of the cycle. In this case the melting took please as consequence of an increase in temperature and radiation (Figure S5). The LMo map for the second melting cycle of this year (Figure 6 C-2) took place during the winter months. Therefore, the colder temperature during this month reduced the number of wet-snow pixels during this cycle (non-white pixels in the LMo' maps). Again, the pixels on lower elevation were those which contributed first to the melting runoff. These LMs were classified also as LM Type III. It is interesting to highlight that some pixels at high elevation also reached their LMo at the beginning of the melting cycle. This LMo were classified as Type II, that is the LM is reached just after the snowfall, but the melting process stopped by a colder temperature refreezes the liquid water in the snowpack. Finally, the third cycle (Figure 6 C-3) showed the expected behavior of a spring melting cycle with a clear increase in radiation and temperature during the melting cycle (Figure A5). The LMo was delayed with elevation, the later the LMo took place the higher its location was. All LMo in this cycle corresponded to LM Type I.

The behavior of melting cycles of the hydrological year 2017-2018 differed from those described for 2016-2017. In this case, three complete snow cycles took place, that is, snow completely disappeared after each of them. Snowfall took place at the beginning of each cycle followed by an increasing pattern in radiation and temperature that favored the melting (Figure A6). Just small-isolated snow patches remained at high elevation during C-1 and C-2. The three LMo maps showed a direct correlation between LMo date and elevation. C-1 (Figure 7 c-1) and C-2 (Figure 7 c-2) took place at the beginning of the winter. The relatively small snowfall in these cycles about 30 mm (Table 3), and the mild temperatures, from 0 ºC to 7.5 ºC, produced shallow snowpacks that quickly melted.

Preprints (www.preprints.org) | NOT PEER-REVIEWED | Posted: 25 September 2023 doi:10.20944/preprints202309.1582.v1

LMo for pixels in low elevation followed the typology of LM Type III. On the contrary, LMo in high elevation were better characterized as LM Type I. The third cycle (Figure 7 C-3) clearly followed the common patterns of a spring melting cycle. It is interesting to highlight that the snow accumulated in this melting cycle occurred in two separate events. The first took place in the whole catchment while the second just on higher elevation. Therefore, LMo at low elevation corresponded to the snowpack of the first snowfall event, while LMo at high elevation corresponded to snowpack accumulated from both snowfall events. Therefore, we can say that LMo and low elevation corresponded to LM Type III and LM at higher elevation to LM Type I. Isolated pixels at higher elevation show LMo corresponding to initial dates and therefore they can be classified as LM Type II (orange pixels at high elevation).

Four melting cycles were identified in the third analyzed year 2018-2019 (Figure 8). While the duration of these cycles was generally longer than in 2017-2018, the total snowfall amount in each of them was much lower. That drove into shallower snowpacks than in previous years that lasted longer due to their timing, earlier in the year, and the lower temperatures than in 2017-2018 (Table 3). The correlation between LMo date and elevation, as in previous years, was also found. This general pattern was not followed by some isolated pixels at high elevations. As in previous years, these LMo appeared just after the snowfall and were initially melted due to an energy exchange between old and new snow (LM Type II), that then refroze due to a snowpack cooling down.

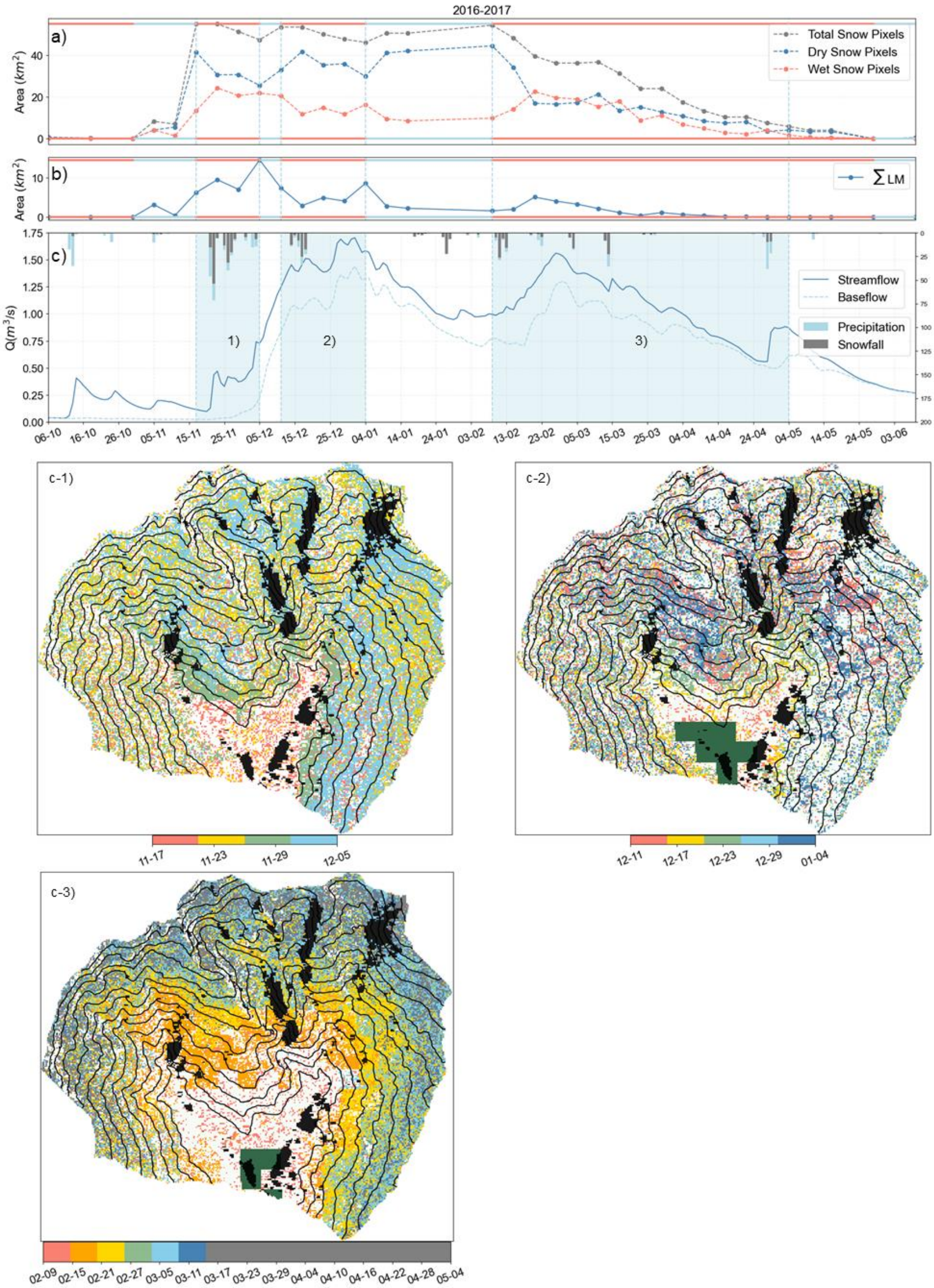

Figure 2. Temporal evolution of analyzed variables for the hydrological year 2018-2019 (a) Total area of snow pixels (grey line), dry snow pixels (blue line) and wet snow pixels (red line). Lines in the top and bottom of every panel identify an accumulation (blue) or melting (red) phase based on the MOD10A2 product. (b) temporal evolution of LM Summatory (blue line). (c) precipitation (blue bars) and snowfalls (gray bars) and the evolution of discharge (blue line), baseflow (dash blue line) and direct runoff (grey line) In all panels, the different melting cycles are highlighted by using a blue rectangle.

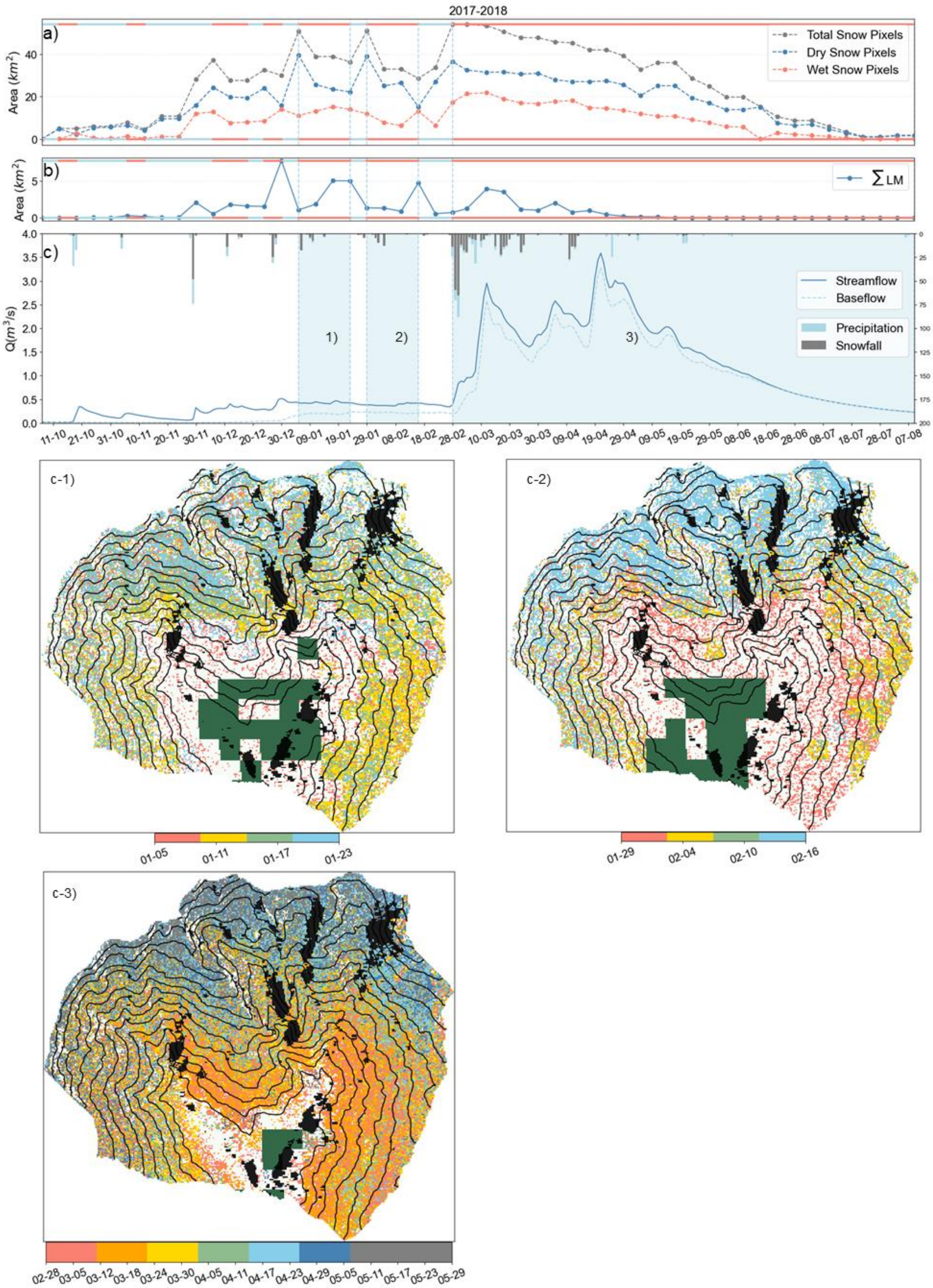

Figure 3. Temporal evolution of analyzed variables for the hydrological year 2018-2019 (a) Total area of snow pixels (grey line), dry snow pixels (blue line) and wet snow pixels (red line). Lines in the top and bottom of every panel identify an accumulation (blue) or melting (red) phase based on the MOD10A2 product. (b) the temporal evolution of the grouped temporally LM (blue line). (c) precipitation (blue bars) and snowfalls (gray bars) and the evolution of discharge (blue line), baseflow (dash blue line) and direct runoff (grey line) In all panels, the different melting cycles are highlighted by using a blue rectangle.

Preprints (www.preprints.org) | NOT PEER-REVIEWED | Posted: 25 September 2023 doi:10.20944/preprints202309.1582.v1

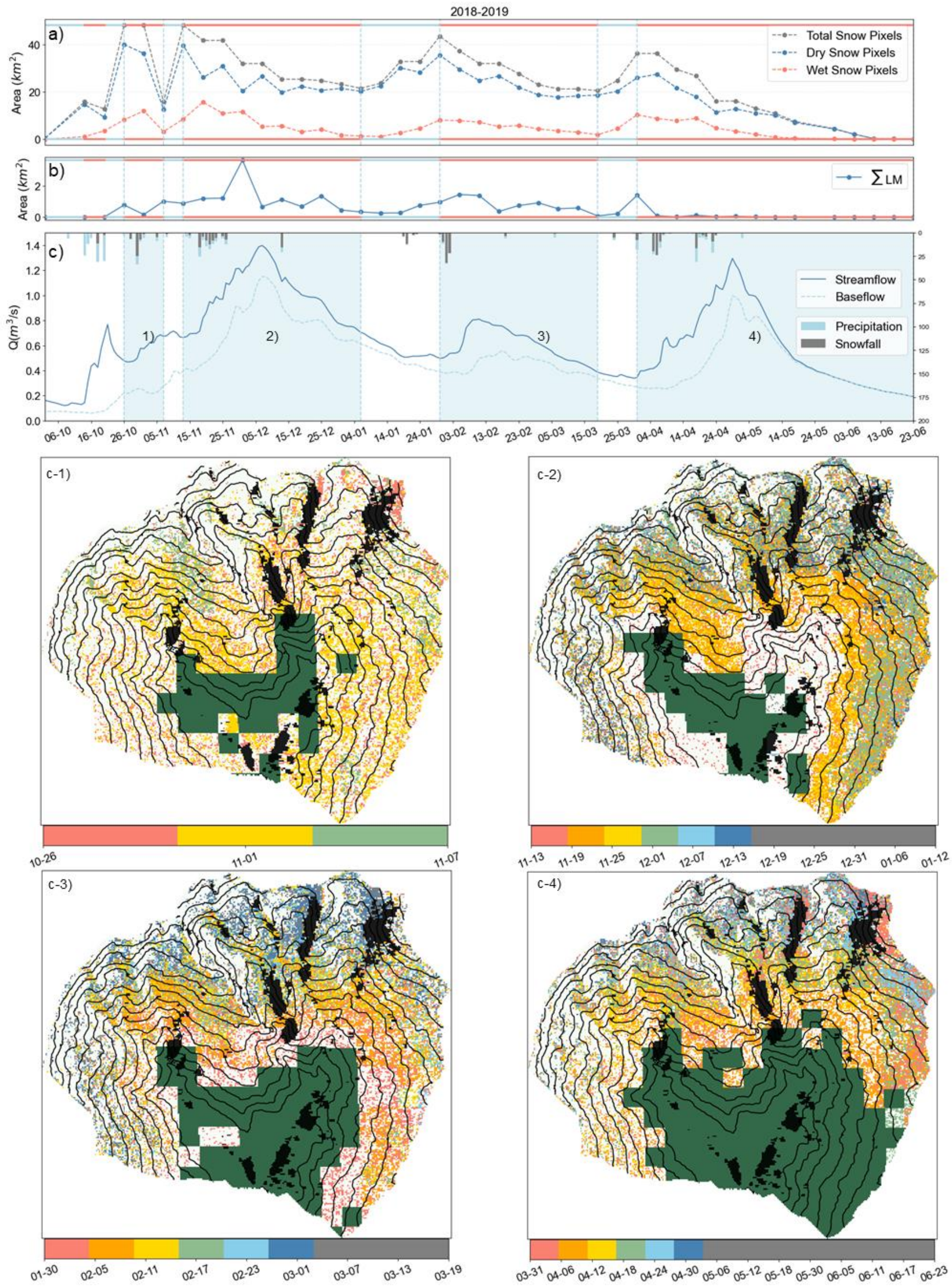

Figure 8. Temporal evolution of analyzed variables for the hydrological year 2018-2019 (a) Total area of snow pixels (grey line), dry snow pixels (blue line) and wet snow pixels (red line). Lines in the top and bottom of every panel identify an accumulation (blue) or melting (red) phase based on the MOD10A2 product. (b) the temporal evolution of the grouped temporally LM (blue line). (c) precipitation (blue bars) and snowfalls (gray bars) and the evolution of discharge (blue line), baseflow (dash blue line) and direct runoff (grey line) In all panels, the different melting cycles are highlighted by using a blue rectangle.

4.2. Wet Snow and Streamflow Interaction

Preprints (www.preprints.org) | NOT PEER-REVIEWED | Posted: 25 September 2023 doi:10.20944/preprints202309.1582.v1

To understand better how wet-snow dynamics is connected to baseflow, a depletion curve was drawn. Only melting cycles with a duration higher than 50 days were chosen for this analysis, thus supporting the representativeness of the analysis having at enough S1-SAR images per analyzed cycle.

All these curves show a similar shape that can be described like a piecewise function composed by three parts (Figure 9):

- Part 1 is represented by a linear an almost horizontal function. Here, there is a high increase in the number of wet snow pixels with almost no change in baseflow response. Hence, this part reflects the delay observed between the beginning of the melting period and the actual response in the river.
- Part 2 can be represented by a power function. In this case, there is an increasing pattern in both variables, which means that both processes, the melting and the baseflow response were occurring at the same time.
- Part 3 follows again a linear function, but in this case, with a vertical pattern. Therefore, the behavior here is the opposite than in Part 1, that is, we observe an increase in baseflow with limited contribution of wet snow pixels. Then, this part represents the time when almost no contribution from wet snow is happening but baseflow is still contributing to the streamflow.

The black symbols over the curves verified this temporal pattern. For example, in the blue curve that represents the 2017-2018, each of them marks the 25% (●), 50% (x) and 75% (+) of the total time of each cycle. These black symbols are almost aligned in all curves and marks approximately for each case the beginning and end of the three parts of the piecewise function explained above.

Moreover, and despite observing this common shape for all curves, these three defined parts were smoothed towards a unique linear pattern when we move from right (brown curve) to left (blue curve) in Figure 9. These differences are connected to the total amount of snow storage during the accumulation period of each melting cycle. For the same number of wet snow pixels, the blue curve generates a considerably higher amount of baseflow than the brown curve. Since S-1 SAR imagery was able to detect wet-snow pixels but not the total liquid content stored in the snowpack, the observed patterns suggested that SWE in the blue curve was higher than in the brown one. When analysing the maximum SWE achieved in each of the accumulation cycles that preceded each of the analysed melting cycles, this hypothesis was verified. Blue curve had a maximum SWE of 184 mm while brown one just reached 43 mm (Table 3). Extending this analysis to the rest of the cycles, we observed that the pattern is fulfilled, from left to right, blue (184 mm), green (78 mm), orange (61 mm), purple (52 mm) and brown (43 mm). That is, the higher the maximum SWE achieved in the snow cycle, the more linear relationship between wet snow pixels contributing to the runoff and baseflow is found. This pattern was also verified when analyzing the time when the peak in baseflow was achieved for each cycle (red triangles over each curve in Figure 10). Lower number of wet snow pixels generating runoff were needed to achieve the maximum baseflow peak.

Finally, to verify our findings we analyzed a totally independent melting cycle from a fourth hydrological year, 2019-2020. This cycle had a duration of 78 days, from 19/03/2020 to 05/06/2020, and a maximum SWE of 50 mm. The shape followed similar pattern than previous melting cycles. Moreover, it had similar timing and a maximum SWE and hence, it was placed close to the purple curve, which reached a maximum SWE of 52 mm.

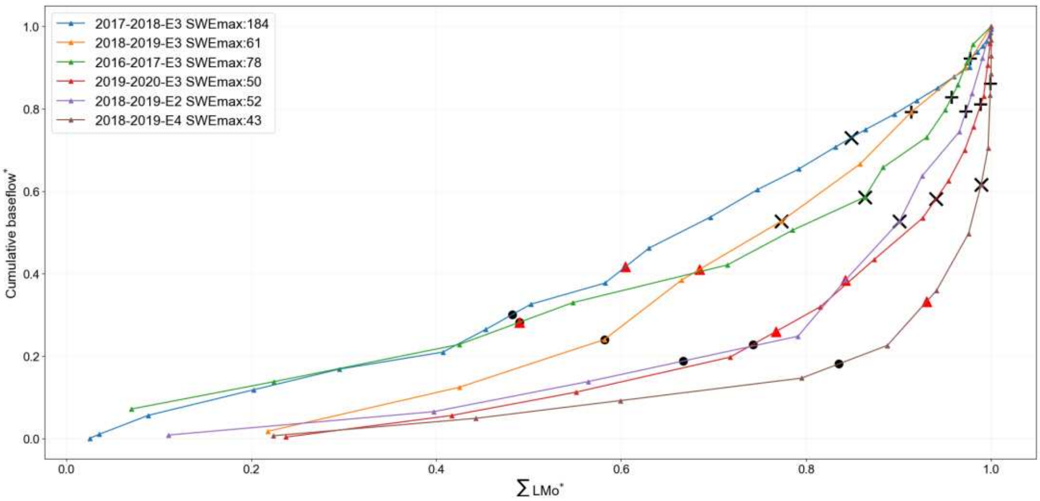

Figure 9. Depletion curves. the x-axis represents the dimensionless cumulative number of pixels contributing to melting runoff in each cycle (ΣLMo). The y-axis represents the dimensionless cumulative baseflow during each cycle. The 2016-2017 event is represented by the green lines. The 2017-2018 event is represented by the blue lines. The 2018-2019 events are represented by the purple line, the orange and brown line. The validation 2019-2020 event is represented by the red line. SWE max value for each cycle is also included in the legend. Red triangles represent the peak in baseflow during each event. Black dots represent the 25 % (●) of the total time of each cycle, black crosses represent 50% (x) of the total time of each cycle. and black plusses represent 75% (+) of the total time of each cycle.

The linear relationship found for long-lasting melting cycles was explored deeply to analyze the potential of S-1 SAR imagery to foresee streamflow dynamics. Previous studies in the area highlighted that despite the absence of aquifers in a strict sense, the highly fractured nature of the lithology results in a highly permeable surface structure that delays snowmelt water inflow into the river [82]. To analyze this delay, we used two variables that can be computed in near-real time: the number of wet snow pixels, which represented the melting dynamics, and the baseflow at the outlet of the catchment which represented the streamflow response. Then, for each melting cycle, we calculated this delay as the number of days between the date when the number of wet snow pixels was maximum and the date when maximum baseflow was achieved. A delay of 21, 13 and 30 days for each of the three cycles was found respectively. After applying this delay, correlation between wet snow pixels and baseflow was computed using the determination coefficient (R^2) (Figure 10). R2 ranged between 0.62 and 0.83. Therefore, a linear relationship was hypothesized between the variables (Figure 10). The slope of the line (baseflow/number of wet snow pixels) indicates the speed of wet snow pixels transform into baseflow. Shorter melting cycles implies lower slope, that is lower speed. This finding is in line with previous results, where the maximum baseflow peak (red triangles in Figure 9) was observed earlier in cycles with higher maximum SWE than in those with a lower maximum SWE.

Preprints (www.preprints.org) | NOT PEER-REVIEWED | Posted: 25 September 2023 doi:10.20944/preprints202309.1582.v1

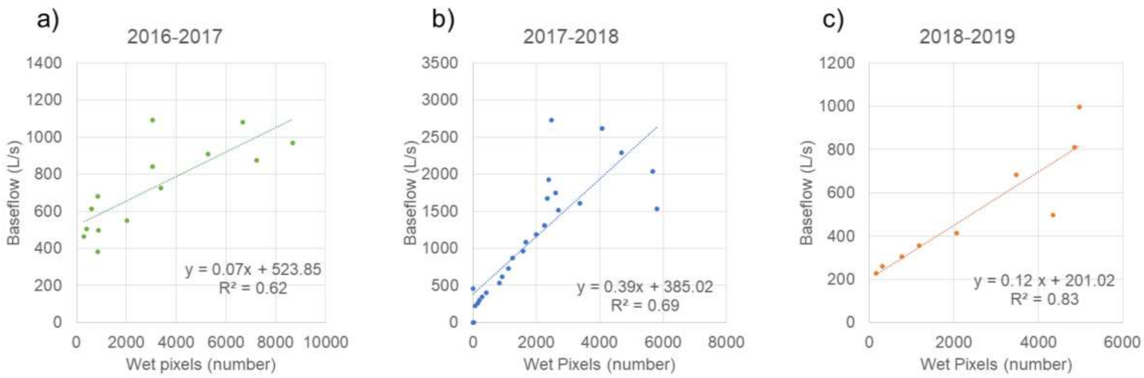

Figure 10. Baseflow and wet snow pixels temporal relationship. The x axis represents the number of wet snow pixels, the y axis represents the corresponding value of the base flow with its respective applied delay. (a) (b) (b).

5. Discussion

The capability of S-1 SAR imagery to improve the understanding of wet snow dynamics over Mediterranean mountain areas was tested. We successfully connected melting dynamics with changes in the backscattering signal by applying the principles stated by [28]. On top of that, we applied this approach not only to the final spring melting but also along all melting cycles that commonly appear throughout the year in these types of environments.

The characteristic of snow over these environments implied some technical challenges when adapting the general methodology to retrieve wet snow from SAR imagery. One of these challenges was the selection of a suitable reference image to remove common ground features that interfere in wet-snow detection. The lack of a long-lasting winter accumulation made difficult to find a full dry snow image, like commonly used in other studies [61,72]. Therefore, the selection of a dry summer image was chosen as reference. Several options were investigated following other authors [83,84]. Among them we observed that the soil dryness during summer month over our target catchments made almost no differences in the use of these different approaches.

Another issue was the definition of the threshold in the Δσ signal to discriminate wet snow. Here a value of -3.00 dB was chosen based on a wet-dry histogram analysis in the target area. This value agrees with other studies in alpine regions such as Austria or Argentina [57,72]. Another example of the use of a similar threshold is found in the Patagonian range in Argentina, a mountain closer to the Mediterranean than to the Alpine snow characteristics [77]. These findings are also in line with the threshold defined by [85–87], where wet snow was successfully analyzed in very different zones such as Finland or Canada. In addition, conditions such as the angle of incidence or the roughness of the snow also play an important role, in our case, angles of incidence of 35°-36° are in close proximity to the 30° analyzed by [88], where the presence of snowpacks with high surface roughness were defined as an optimal range of values to define wet snow. In our case the shallow snowpack and the high snow roughness after some wind episodes visible in the terrestrial imagery support the selection of this threshold.

It is interesting to highlight that we have just used one of the two available orbits, which take place during the same day at different timing. Future analyses in the area should incorporate both orbits, being in this way able to capture hydrological differences between morning and evening snowpack. This daily changes are frequent in Mediterranean mountain like Sierra Nevada, especially during spring melting [28].

The use of terrestrial photography also helped to deeply interpreted Δσ signal at the local scale. We were able to identify four types of LMs that triggered snowmelt-onset based on the classification proposed by [3]. These LMs had different values depending on their timing throughout the year. This confirms the heterogeneity of the area, which can have different snowfalls events throughout the year, which ends up implying that we do not always have the minimum $\Delta\sigma$ values in the long-lasting spring melting cycles.

This understanding of wet-snow dynamics helps to comprehend the melting-runoff onset maps at the catchment scale, which constitutes a useful tool for water managers to know the distribution of the melting dynamics. One limitation of these maps is that they are computed at the end of the snow season. They can be used to understand snow behavior but not to foresee changes in advance. On the contrary, the relationships found in section 4.2 goes a step further being able to be computed in quasireal real-time. On the one hand the depletion curves, with a common shape, defined a space where streamflow response and wet snow dynamics are linked using the maximum SWE of the analyzing melting cycle. Hence, knowing the maximum SWE achieved during the accumulation, a hypothetical curve can be drawn over this space to anticipate streamflow behavior. On the other hand, a mean delay of 21 days, between the beginning of the melting-runoff and streamflow peak was identified, narrowing down the water manager time to foresee runoff melting impact on the streamflow. More specifically, the proposed methodology can be applied in other sub-basins and be incorporated in operational hydrological modeling systems [89–91].

6. Conclusions

The interpretation of SAR backscattering is not always straightforward, especially in regions where snowpacks are shallow and not permanent throughout the snow season, like in Mediterranean mountain areas as Sierra Nevada. In this work, we analyzed snow dynamics and their relationship with streamflow response in such semiarid mountains using S-1 SAR imagery. The main conclusions are the following:

- Regarding methodology for wet-snow dynamics identification, S-1 SAR imagery was able not only to capture the final spring melting but also all melting cycles that commonly appear throughout the year in these types of environments. The general change detection approach used in other regions to identify wet snow was successfully adapted to be applied in semiarid mountains. The main changes carried out were the selection of an average S-1 SAR image from all images during the previous summer, and the definition of a wet snow threshold of -3.00 dB.
- Regarding backscattering understanding, the analysis at the local scale allows us to define four different type of melting runoff onsets triggering the melting. Each of them was associated to a specific type of melting cycle which was also connected to specific snowpack characteristics (e.g., snowpack depth, duration of the accumulation phase before the melting cycle, time of the year).
- At the catchment scale, a new approach was proposed for defined melting cycles throughout the year by using just S-1 SAR imagery. Using that, distributed melting runoff onset maps were obtained to better understand the spatiotemporal evolution of melting dynamics.
- Regarding the connection between snowmelt dynamics and streamflow, a common piecewise function, composed by three parts, was found to explain it. The shape of this curve was directly connected to the maximum SWE achieved during the snow cycle. The higher the SWE the more linear this relation was. This linear relationship for long-lasting melting cycles was used to find a mean delay between the melting onset and streamflow peak of about 21 days.

This work constitutes a first approach to better understand S-1 SAR imagery backscattering and assess its capability to foresee changes in streamflow over Mediterranean mountains. As next step we intend to improve the interpretation at the local scale by using, in addition to terrestrial imagery, measured variables such as SWE or temperature at different heights of the snow cover as well as the morning acquisitions of S-1 data. These potential improvements will help to achieve better interpretations of the snowpack dynamics in this type of environment and therefore improve our predictive capacity of streamflow in the area.

Acknowlegments: This study was supported and partially funded by the Spanish Ministry of Science and Innovation through the research projects PID2021-12323SNB-I00, HYPOMED - "Incorporating hydrological uncertainty and risk analysis to the operation of hydropower facilities in Mediterranean mountain watersheds").

 doi:10.20944/preprints202309.1582.v1

P. Torralbo acknowledges fundings by the Ayudas para la formación de profesorado universitario (FPU) (Convocatoria 2017) the Spanish Ministry of Education, Culture and Sports (FPU17/01003). P. Torralbo, R. Pimentel, and M.J. Polo are members of DAUCO, Unit of Excellence ref. CEX2019–000968-M, with financial support from the Spanish Ministry of Science and Innovation, the Spanish State Research Agency, through the Severo Ochoa and María de Maeztu Program for Centers and Units of Excellence in R&D. The authors would like to thank Eurac Research, particularly to Institute for Earth Observation as it allowed P. Torralbo for stay during the summer of 2021, which has been fundamental for this work.

Conflicts of Interest: The authors declare no conflict of interest.

Appendix A. Sensitivity Analysis

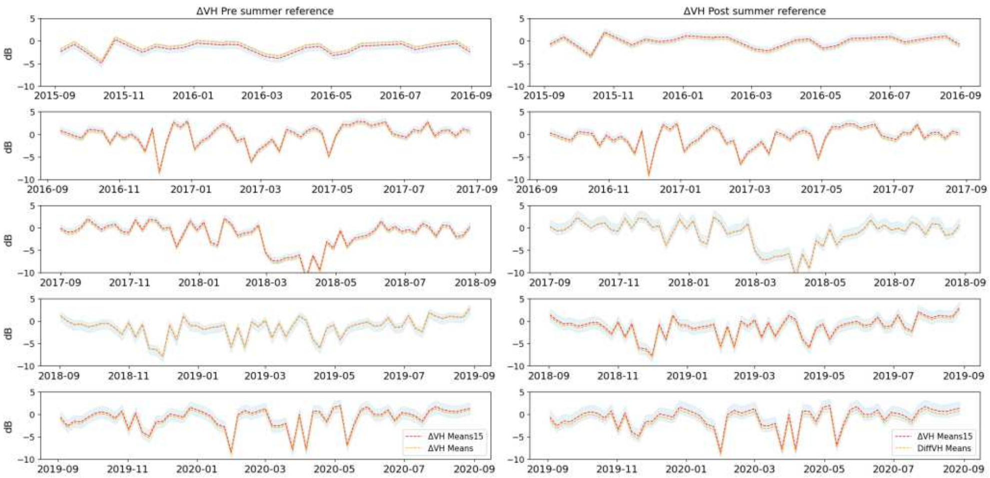

Figure A1. Sensitivity analysis of each of the hydrological years. The blue area represents the range of values for each of the summer images used independently. The red line represents the value obtained using the mean of the images that meet the criterion of 15 days without previous precipitation during the summer. The blue line represents the value obtained using the average of all summer images.

Local Scale: Wet Snow Threshold definition

The selected days have been the following scenes i) 2016-12-05, ii)2017-03-05, iii) 2018-02-16, iv)2018-2-28, v) 2019-04-12 and vi) 2019-04-24. These images have been chosen based on the existence of possible dry, wet snow pixels and non-snow pixels. All the scenes have been previously filtered using the image of 8 days MODIS that considers the specific image.

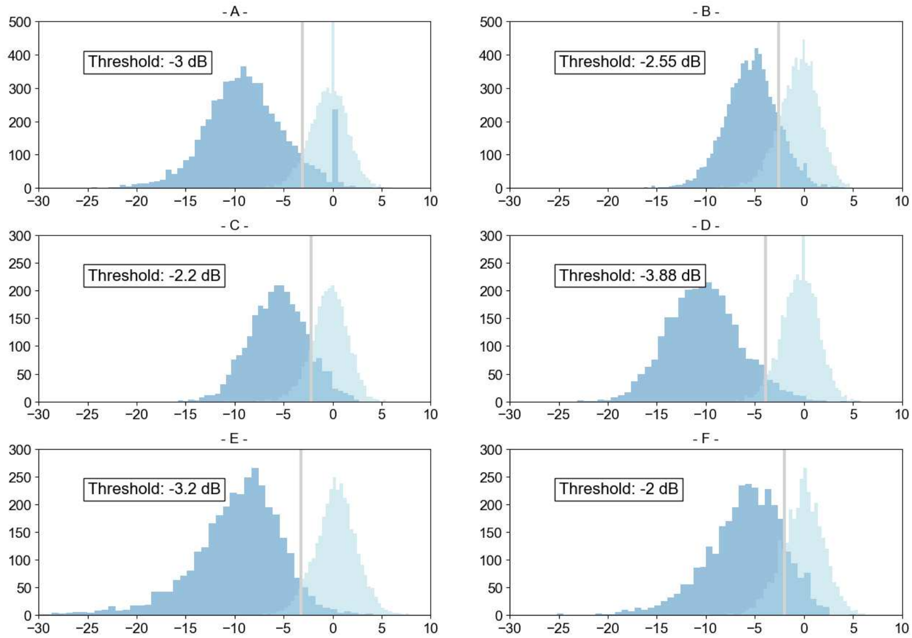

Figure A2. Graph A to F represent the overlapping distribution of wet snow pixels and snowless pixels for different periods.

Local Scale: Backscatter signal understanding - Terrestrial images

Preprints (www.preprints.org) | NOT PEER-REVIEWED | Posted: 25 September 2023 doi:10.20944/preprints202309.1582.v1

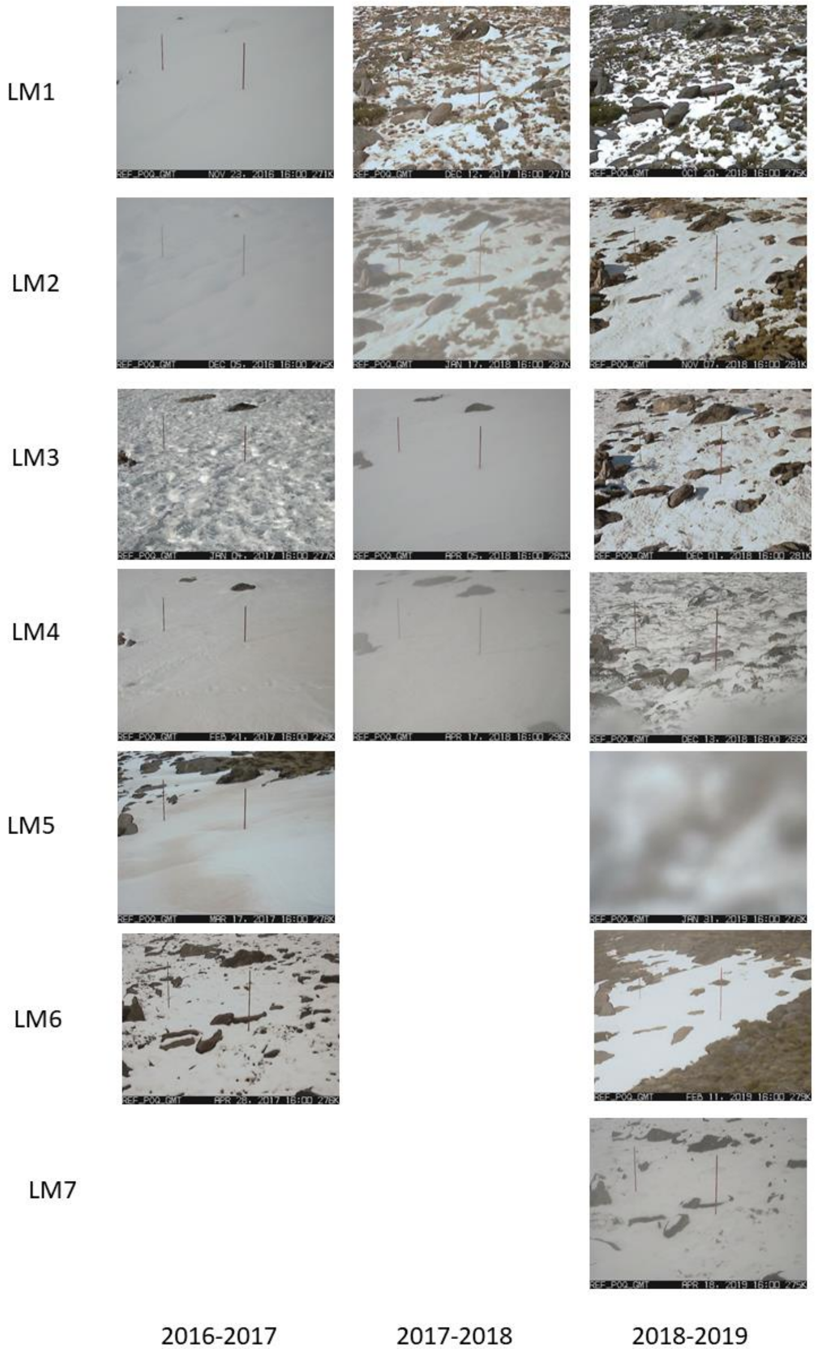

Figure A3. Local scale images (Refugio Poqueira) coinciding with the local minima obtained with the S-1 SAR image for each of the three years analyzed.

Catchment Scale: Analysis of the impact of meteorological variables on LMo

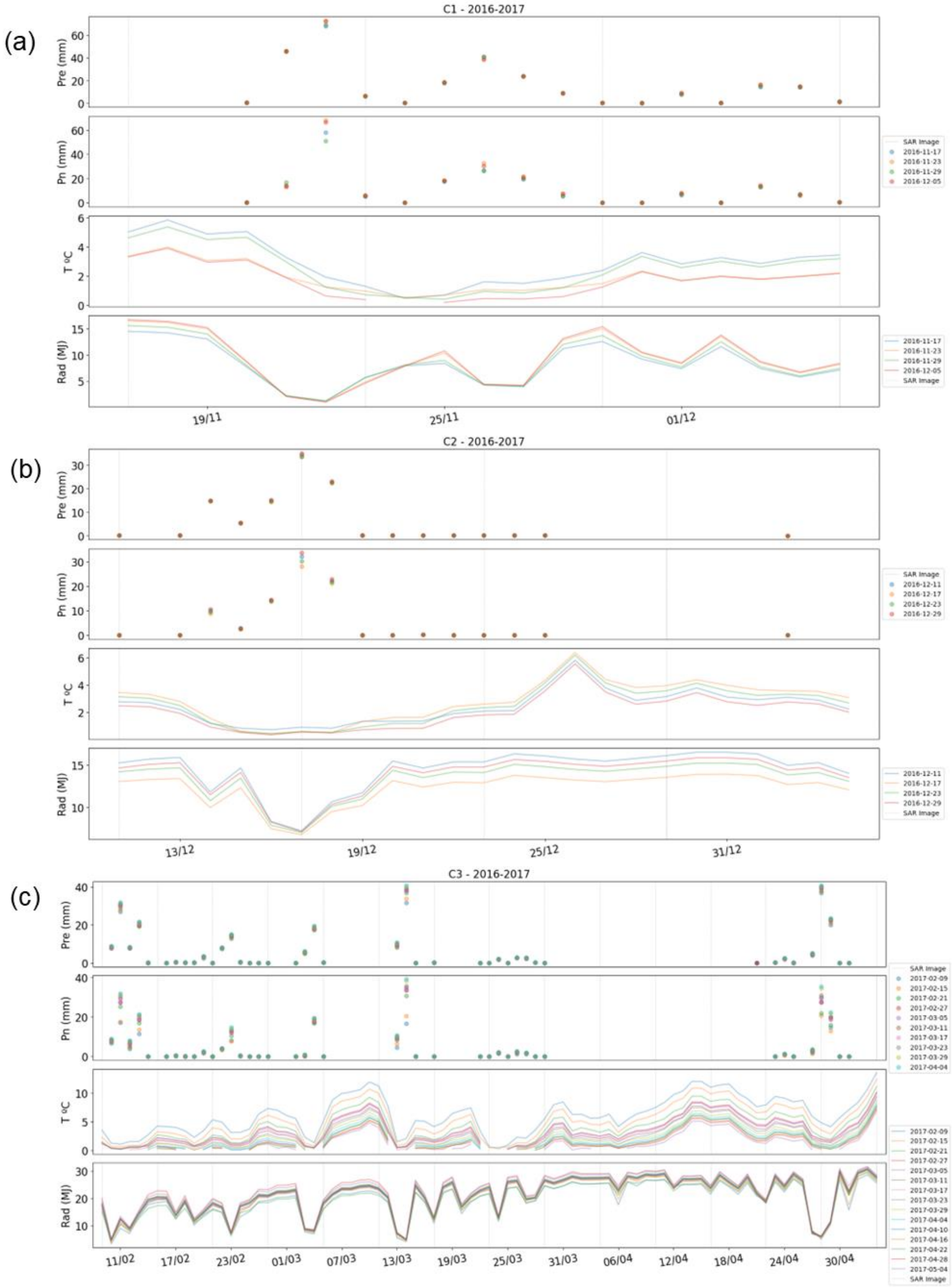

Figure A4. Temporal evolution of analyzed variables for the hydrological year 2016-2017; (i) precipitation, (ii) snowfall, (iii) temperature, and (iv) radiation. Every graph represents the average value of the given variable for all the pixels in every LMo. (a) Temporal evolution of LMo pixels for Cycle I, (b) Temporal evolution of LMo pixels for Cycle II, (c) Temporal evolution of LMo pixels for Cycle III. Vertical lines indicate the day on which we have S-1 SAR image.

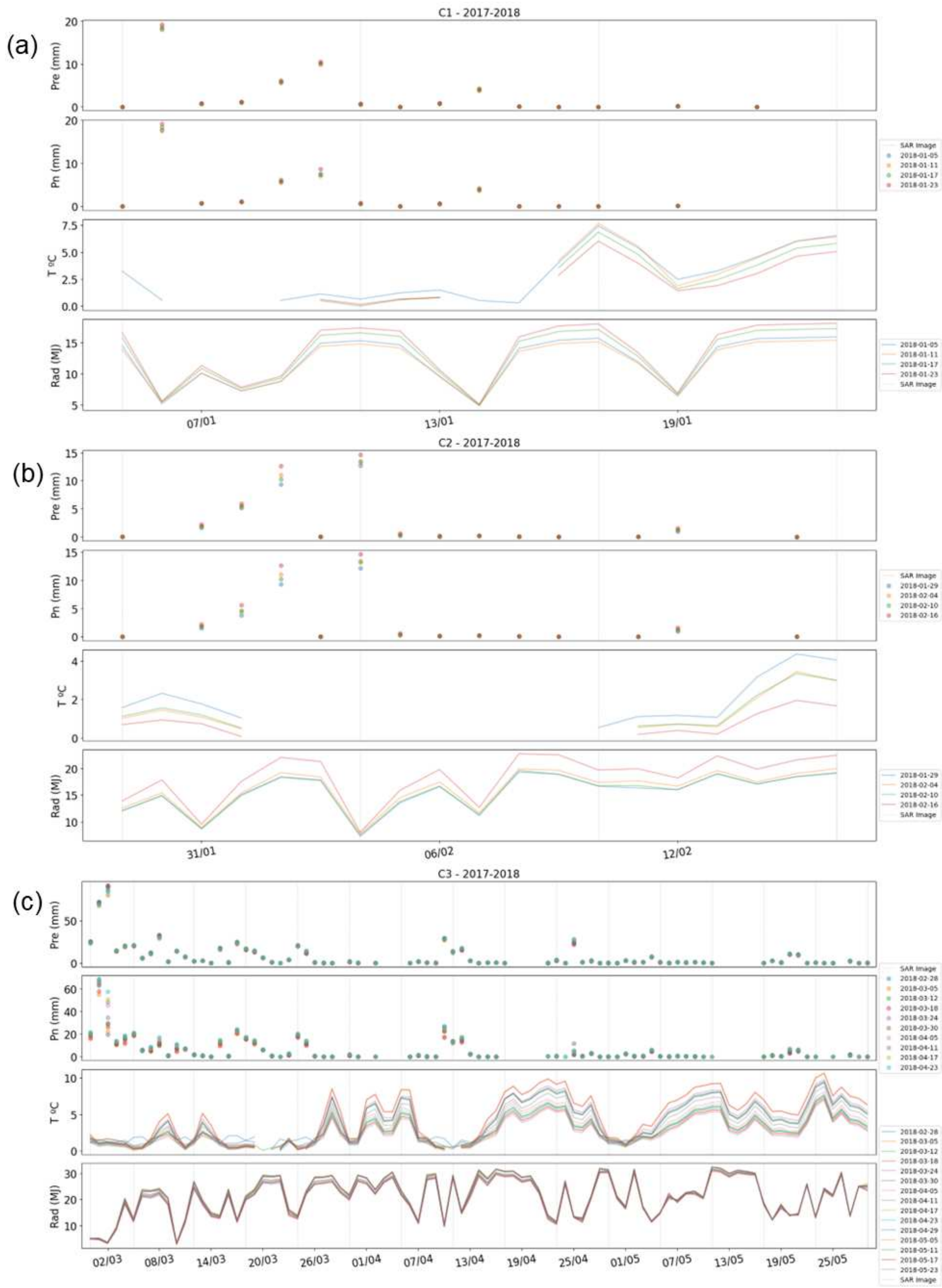

Figure A5. Temporal evolution of analyzed variables for the hydrological year 2017-2018; (i) precipitation, (ii) snowfall, (iii) temperature, and (iv) radiation. Every graph represents the average value of the given variable for all the pixels in every LMo. (a) Temporal evolution of LMo pixels for Cycle I, (b) Temporal evolution of LMo pixels for Cycle II, (c) Temporal evolution of LMo pixels for Cycle III. Vertical lines indicate the day on which we have S-1 SAR image.

References

1. Allan, R.P.; Barlow, M.; Byrne, M.P.; Cherchi, A.; Douville, H.; Fowler, H.J.; Gan, T.Y.; Pendergrass, A.G.; Rosenfeld, D.; Swann, A.L.S.; et al. Advances in Understanding Large-Scale Responses of the Water Cycle to Climate Change. *Ann. N. Y. Acad. Sci.* 2020, *1472*.
2. Polo, M.J.; Pimentel, R.; Gascoin, S.; Notarnicola, C. Mountain Hydrology in the Mediterranean Region. *Water Resour. Mediterr. Reg.* **2020**, 51–75, doi:10.1016/B978-0-12-818086-0.00003-0.
3. Pimentel, R.; Herrero, J.; Polo, M.J. Subgrid Parameterization of Snow Distribution at a Mediterranean Site Using Terrestrial Photography. *Hydrol. Earth Syst. Sci.* **2017**, *21*, 805–820, doi:10.5194/hess-21-805-2017.
4. Pimentel, R.; Herrero, J.; Polo, M. Quantifying Snow Cover Distribution in Semiarid Regions Combining Satellite and Terrestrial Imagery. *Remote Sens.* **2017**, *9*, 995, doi:10.3390/rs9100995.

5. Fayad, A.; Gascoin, S.; Faour, G.; Fanise, P.; Drapeau, L.; Somma, J.; Fadel, A.; Al Bitar, A.; Escadafal, R. Snow Observations in Mount Lebanon (2011-2016). *Earth Syst. Sci. Data* **2017**, *9*, doi:10.5194/essd-9-573-2017.
6. Herrero, J.; Polo, M.J. Evaposublimation from the Snow in the Mediterranean Mountains of Sierra Nevada (Spain). *Cryosph.* **2016**, *10*, 2981–2998, doi:10.5194/tc-10-2981-2016.
7. Thakur, P.K.; Garg, V.; Nikam, B.R.; Singh, S.; Chouksey, A.; Dhote, P.R.; Aggarwal, S.P.; Chauhan, P.; Kumar, A.S. SNOW COVER AND GLACIER DYNAMICS STUDY USING C-AND L-BAND SAR DATASETS IN PARTS OF NORTH WEST HIMALAYA. *Int. Arch. Photogramm. Remote Sens. Spat. Inf. Sci.* **2018**, *XLII–5*, 375–382, doi:10.5194/isprs-archives-XLII-5-375-2018.
8. Contreras, E.; Herrero, J.; Crochemore, L.; Aguilar, C.; Polo, M.J. Seasonal Climate Forecast Skill Assessment for the Management of Water Resources in a Run of River Hydropower System in the Poqueira River (Southern Spain). *Water (Switzerland)* **2020**, *12*, doi:10.3390/W12082119.
9. Gray, D.; McKay, G. The Handbook of Snow: Principles, Processes, Management & Use; 1981;
10. DeWalle, D.R.; Rango, A. *Principles of Snow Hydrology*; Cambridge University Press, 2008; ISBN 9780521823623.
11. House, A. Corrigendum to: Physical Hydrology By S. Lawrence Dingman [Hydrological Sciences Journal, (2015), 643]. *Hydrol. Sci. J.* 2015, *60*.
12. Elder, K.; Dozier, J.; Michaelsen, J. Snow Accumulation and Distribution in an Alpine Watershed. *Water Resour. Res.* **1991**, *27*, doi:10.1029/91WR00506.
13. Egli, L.; Jonas, T.; Meister, R. Comparison of Different Automatic Methods for Estimating Snow Water Equivalent. *Cold Reg. Sci. Technol.* **2009**, *57*, doi:10.1016/j.coldregions.2009.02.008.
14. Domine, F. Physical Properties of Snow. In Proceedings of the Encyclopedia of Earth Sciences Series; 2011; Vol. Part 3.
15. Colbeck, S.C. An Overview of Seasonal Snow Metamorphism. *Rev. Geophys.* 1982, *20*.
16. Kinar, N.J.; Pomeroy, J.W. Measurement of the Physical Properties of the Snowpack. *Rev. Geophys.* 2015, *53*.
17. Pirazzini, R.; Leppänen, L.; Picard, G.; Lopez-Moreno, J.I.; Marty, C.; Macelloni, G.; Kontu, A.; von Lerber, A.; Tanis, C.M.; Schneebeli, M.; et al. European In-Situ Snow Measurements: Practices and Purposes. *Sensors (Switzerland)* **2018**, *18*, doi:10.3390/s18072016.
18. Helbig, N.; Schirmer, M.; Magnusson, J.; Mäder, F.; Van Herwijnen, A.; Quéno, L.; Bühler, Y.; Deems, J.S.; Gascoin, S. A Seasonal Algorithm of the Snow-Covered Area Fraction for Mountainous Terrain. *Cryosphere* **2021**, *15*, doi:10.5194/tc-15-4607-2021.
19. Riggs, G.; Hall, D. MODIS Snow Products Collection 6 User Guide. *Natl. Snow Ice Data Cent. Distrib. Act. Arch. Cent.* 2016.
20. Bair, E.H.; Rittger, K.; Skiles, S.M.K.; Dozier, J. An Examination of Snow Albedo Estimates From MODIS and Their Impact on Snow Water Equivalent Reconstruction. *Water Resour. Res.* **2019**, *55*, doi:10.1029/2019WR024810.
21. Pimentel, R.; Aguilar, C.; Herrero, J.; Pérez-Palazón, M.J.; Polo, M.J. Comparison between Snow Albedo Obtained from Landsat TM, ETM+ Imagery and the SPOT VEGETATION Albedo Product in a Mediterranean Mountainous Site. *Hydrology* **2016**, *3*, doi:10.3390/hydrology3010010.
22. Painter, T.H.; Rittger, K.; McKenzie, C.; Slaughter, P.; Davis, R.E.; Dozier, J. Retrieval of Subpixel Snow Covered Area, Grain Size, and Albedo from MODIS. *Remote Sens. Environ.* **2009**, *113*, doi:10.1016/j.rse.2009.01.001.
23. Takala, M.; Luojus, K.; Pulliainen, J.; Derksen, C.; Lemmetyinen, J.; Kärnä, J.P.; Koskinen, J.; Bojkov, B. Estimating Northern Hemisphere Snow Water Equivalent for Climate Research through Assimilation of Space-Borne Radiometer Data and Ground-Based Measurements. *Remote Sens. Environ.* **2011**, *115*, 3517–3529, doi:10.1016/J.RSE.2011.08.014.
24. Tsang, L.; Durand, M.; Derksen, C.; Barros, A.P.; Kang, D.H.; Lievens, H.; Marshall, H.P.; Zhu, J.; Johnson, J.; King, J.; et al. Review Article: Global Monitoring of Snow Water Equivalent Using High-Frequency Radar Remote Sensing. *Cryosphere* 2022, *16*.
25. Venäläinen, P.; Luojus, K.; Mortimer, C.; Lemmetyinen, J.; Pulliainen, J.; Takala, M.; Moisander, M.; Zschenderlein, L. Implementing Spatially and Temporally Varying Snow Densities into the GlobSnow Snow Water Equivalent Retrieval. *Cryosphere* **2023**, *17*, doi:10.5194/tc-17-719-2023.
26. Walker, A.E.; Goodison, B.E. Discrimination of a Wet Snow Cover Using Passive Microwave Satellite Data. *Ann. Glaciol.* **1993**, *17*, doi:10.1017/s026030550001301x.
27. Ulaby, F.T.; Stiles, W.H.; Dellwig, L.F.; Hanson, B.C. Experiments on the Radar Backscatter of Snow. *IEEE Trans. Geosci. Electron.* **1977**, *15*, doi:10.1109/TGE.1977.294490.
28. Marin, C.; Bertoldi, G.; Premier, V.; Callegari, M.; Brida, C.; Hürkamp, K.; Tschiersch, J.; Zebisch, M.; Notarnicola, C. Use of Sentinel-1 Radar Observations to Evaluate Snowmelt Dynamics in Alpine Regions. *Cryosph.* **2020**, *14*, 935–956, doi:10.5194/tc-14-935-2020.

29. Antropova, Y.K.; Komarov, A.S.; Richardson, M.; Millard, K.; Smith, K. Detection of Wet Snow in the Arctic Tundra from Time-Series Fully-Polarimetric RADARSAT-2 Images. *Remote Sens. Environ.* **2022**, *283*, doi:10.1016/j.rse.2022.113305.
30. Torres, R.; Snoeij, P.; Geudtner, D.; Bibby, D.; Davidson, M.; Attema, E.; Potin, P.; Rommen, B.Ö.; Floury, N.; Brown, M.; et al. GMES Sentinel-1 Mission. *Remote Sens. Environ.* **2012**, *120*, doi:10.1016/j.rse.2011.05.028.
31. Hu, J.; Zhang, T.; Zhou, X.; Jiang, L.; Yi, G.; Wen, B.; Chen, Y. Extracting Time-Series of Wet-Snow Facies in Greenland Using Sentinel-1 SAR Data on Google Earth Engine. *IEEE J. Sel. Top. Appl. Earth Obs. Remote Sens.* **2022**, *15*, doi:10.1109/JSTARS.2022.3192409.
32. Zhu, Q.; Guo, H.; Zhang, L.; Liang, D.; Liu, X.; Zhou, H.; Gou, Y. High-Resolution Spatio-Temporal Analysis of Snowmelt over Antarctic Peninsula Ice Shelves from 2015 to 2021 Using SAR Images. *Int. J. Digit. Earth* **2023**, *16*, doi:10.1080/17538947.2023.2181991.
33. Luo, S.; Xiong, J.; Liu, S.; Hu, K.; Cheng, W.; Liu, J.; He, Y.; Sun, H.; Cui, X.; Wang, X. New Insights into Ice Avalanche-Induced Debris Flows in Southeastern Tibet Using SAR Technology. *Remote Sens.* **2022**, *14*, doi:10.3390/rs14112603.
34. Tramblay, Y.; Koutroulis, A.; Samaniego, L.; Vicente-Serrano, S.M.; Volaire, F.; Boone, A.; Le Page, M.; Llasat, M.C.; Albergel, C.; Burak, S.; et al. Challenges for Drought Assessment in the Mediterranean Region under Future Climate Scenarios. *Earth-Science Rev.* 2020, *210*.
35. Pimentel, R.; Herrero, J.; Zeng, Y.; Su, Z.; Polo, M.J. Study of Snow Dynamics at Subgrid Scale in Semiarid Environments Combining Terrestrial Photography and Data Assimilation Techniques. *J. Hydrometeorol.* **2015**, *16*, doi:10.1175/JHM-D-14-0046.1.
36. Ramage, J.M.; McKenney, R.A.; Thorson, B.; Maltais, P.; Kopczynski, S.E. Relationship between Passive Microwave-Derived Snowmelt and Surface-Measured Discharge, Wheaton River, Yukon Territory, Canada. In Proceedings of the Hydrological Processes; 2006; Vol. 20.
37. Hall, D.K.; Foster, J.L.; DiGirolamo, N.E.; Riggs, G.A. Snow Cover, Snowmelt Timing and Stream Power in the Wind River Range, Wyoming. *Geomorphology* **2012**, *137*, doi:10.1016/j.geomorph.2010.11.011.
38. Godsey, S.E.; Kirchner, J.W. Dynamic, Discontinuous Stream Networks: Hydrologically Driven Variations in Active Drainage Density, Flowing Channels and Stream Order. *Hydrol. Process.* **2014**, *28*, doi:10.1002/hyp.10310.
39. Uzun, S.; Tanir, T.; Coelho, G. de A.; Souza de Lima, A. de; Cassalho, F.; Ferreira, C.M. Changes in Snowmelt Runoff Timing in the Contiguous United States. *Hydrol. Process.* **2021**, *35*, doi:10.1002/hyp.14430.
40. Li, S.; Liu, M.; Adam, J.C.; Pi, H.; Su, F.; Li, D.; Liu, Z.; Yao, Z. Contribution of Snow-Melt Water to the Streamflow over the Three-River Headwater Region, China. *Remote Sens.* **2021**, *13*, doi:10.3390/rs13081585.
41. Blankinship, J.C.; Meadows, M.W.; Lucas, R.G.; Hart, S.C. Snowmelt Timing Alters Shallow but Not Deep Soil Moisture in the Sierra Nevada. *Water Resour. Res.* **2014**, *50*, doi:10.1002/2013WR014541.
42. McNamara, J.P.; Chandler, D.; Seyfried, M.; Achet, S. Soil Moisture States, Lateral Flow, and Streamflow Generation in a Semi-Arid, Snowmelt-Driven Catchment. *Hydrol. Process.* **2005**, *19*, doi:10.1002/hyp.5869.
43. Pérez-Palazón, M.J.; Pimentel, R.; Polo, M.J. Climate Trends Impact on the Snowfall Regime in Mediterranean Mountain Areas: Future Scenario Assessment in Sierra Nevada (Spain). *Water (Switzerland)* **2018**, *10*, doi:10.3390/w10060720.
44. Herrero, J.; Polo, M.J.; Moñino, A.; Losada, M.A. An Energy Balance Snowmelt Model in a Mediterranean Site. *J. Hydrol.* **2009**, *371*, 98–107, doi:10.1016/J.JHYDROL.2009.03.021.
45. Polo, M.J.; Herrero, J.; Pimentel, R.; Pérez-Palazón, M.J. The Guadalfeo Monitoring Network (Sierra Nevada, Spain): 14 Years of Measurements to Understand the Complexity of Snow Dynamics in Semiarid Regions. *Earth Syst. Sci. Data* **2019**, *11*, doi:10.5194/essd-11-393-2019.
46. Aguilar, C.; Herrero, J.; Millares, A.; Losada, M.A.; Polo, M.J. Meteomap: Generation of Meteorological Variables for Distribuited Physically-Based Hydrological Modeling. In Proceedings of the 11th International Conference on Hydroinformatics; 2014.
47. Herrero, J.; Aguilar, C.; Polo, M.J.; Losada, M.Á. Mapping of Meteorological Varaibles for Runoff Generation Forecast in Distributed Hydrological Modeling. In Proceedings of the Hydraulic Measurements & Experimental Methods Conference; 2007.
48. Aguilar, C.; Herrero, J.; Polo, M.J. Topographic Effects on Solar Radiation Distribution in Mountainous Watersheds and Their Influence on Reference Evapotranspiration Estimates at Watershed Scale. *Hydrol. Earth Syst. Sci.* **2010**, *14*, 2479–2494, doi:10.5194/hess-14-2479-2010.
49. Mätzler, C. Applications of the Interaction of Microwaves with the Natural Snow Cover. *Remote Sens. Rev.* **1987**, *2*, doi:10.1080/02757258709532086.
50. Strozzi, T.; Wiesmann, A.; Mätzler, C. Active Microwave Signatures of Snow Covers at 5.3 and 35 GHz. *Radio Sci.* **1997**, *32*, doi:10.1029/96RS03777.
51. PENMAN, H.L. Natural Evaporation from Open Water, Hare Soil and Grass. *Proc. R. Soc. Lond. A. Math. Phys. Sci.* **1948**, *193*, doi:10.1098/rspa.1948.0037.
52. Monteith, J.L.; Szeicz, G.; Yabuki, K. Crop Photosynthesis and the Flux of Carbon Dioxide Below the Canopy. *J. Appl. Ecol.* **1964**, *1*, doi:10.2307/2401316.

53. Heber Green, W.; Ampt, G.A. Studies on Soil Phyics. *J. Agric. Sci.* **1911**, *4*, doi:10.1017/S0021859600001441.
54. Millares, A.; Polo, M.J.; Losada, M.A. The Hydrological Response of Baseflow in Fractured Mountain Areas. *Hydrol. Earth Syst. Sci.* **2009**, *13*, doi:10.5194/hess-13-1261-2009.
55. Pastén-Zapata, E.; Pimentel, R.; Royer-Gaspard, P.; Sonnenborg, T.O.; Aparicio-Ibañez, J.; Lemoine, A.; Pérez-Palazón, M.J.; Schneider, R.; Photiadou, C.; Thirel, G.; et al. The Effect of Weighting Hydrological Projections Based on the Robustness of Hydrological Models under a Changing Climate. *J. Hydrol. Reg. Stud.* **2022**, *41*, doi:10.1016/j.ejrh.2022.101113.
56. Nagler, T.; Rott, H. Snow Classification Algorithm for ENVISAT ASAR. In Proceedings of the European Space Agency, (Special Publication) ESA SP; 2005.
57. Nagler, T.; Rott, H. Retrieval of Wet Snow by Means of Multitemporal SAR Data. *IEEE Trans. Geosci. Remote Sens.* **2000**, *38*, doi:10.1109/36.842004.
58. Nagler, T.; Rott, H.; Ripper, E.; Bippus, G.; Hetzenecker, M. Advancements for Snowmelt Monitoring by Means of Sentinel-1 SAR. *Remote Sens.* **2016**, *8*, doi:10.3390/rs8040348.
59. Ulaby, F.; Long, D. Microwave Radar and Radiometric Remote Sensing; 2014;
60. He, G.; Feng, X.; Xiao, P.; Xia, Z.; Wang, Z.; Chen, H.; Li, H.; Guo, J. Dry and Wet Snow Cover Mapping in Mountain Areas Using SAR and Optical Remote Sensing Data. *IEEE J. Sel. Top. Appl. Earth Obs. Remote Sens.* **2017**, *10*, doi:10.1109/JSTARS.2017.2673409.
61. Snapir, B.; Momblanch, A.; Jain, S.K.; Waine, T.W.; Holman, I.P. A Method for Monthly Mapping of Wet and Dry Snow Using Sentinel-1 and MODIS: Application to a Himalayan River Basin. *Int. J. Appl. Earth Obs. Geoinf.* **2019**, *74*, doi:10.1016/j.jag.2018.09.011.
62. Nagler, T.; Schwaizer, G.; Ossowska, J.; Rott, H.; Small, D. Towards an Advanced Pan-European Snow Cover Product from Sentinel-1 SAR and Sentinel-3 SLSTR. In Proceedings of the EGU 2018; 2018; Vol. 20.
63. Schellenberger, T.; Ventura, B.; Zebisch, M.; Notarnicola, C. Wet Snow Cover Mapping Algorithm Based on Multitemporal COSMO-SkyMed X-Band SAR Images. *IEEE J. Sel. Top. Appl. Earth Obs. Remote Sens.* **2012**, *5*, doi:10.1109/JSTARS.2012.2190720.
64. Gorelick, N.; Hancher, M.; Dixon, M.; Ilyushchenko, S.; Thau, D.; Moore, R. Google Earth Engine: Planetary-Scale Geospatial Analysis for Everyone. *Remote Sens. Environ.* **2017**, *202*, doi:10.1016/j.rse.2017.06.031.
65. Buchelt, S.; Skov, K.; Rasmussen, K.K.; Ullmann, T. Sentinel-1 Time Series for Mapping Snow Cover Depletion and Timing of Snowmelt in Arctic Periglacial Environments: Case Study from Zackenberg and Kobbefjord, Greenland. *Cryosphere* **2022**, *16*, doi:10.5194/tc-16-625-2022.
66. Ulaby, F.T.; Abdelrazik, M.; Stiles, W.H. Snowcover Influence on Backscattering from Terrain. *IEEE Trans. Geosci. Remote Sens.* **1984**, *GE-22*, doi:10.1109/TGRS.1984.350604.
67. Linlor, W.I. Permittivity and Attenuation of Wet Snow between 4 and 12 GHz. *J. Appl. Phys.* **1980**, *51*, doi:10.1063/1.327947.
68. Schreier, G. Geometrical Properties of SAR Images. In *SAR Geocoding: Data and Systems*; 1993.
69. Yin, D.; Cao, X.; Chen, X.; Shao, Y.; Chen, J. Comparison of Automatic Thresholding Methods for Snow-Cover Mapping Using Landsat TM Imagery. *Int. J. Remote Sens.* **2013**, *34*, doi:10.1080/01431161.2013.803631.
70. Zhang, H.; Zhang, F.; Zhang, G.; Che, T.; Yan, W.; Ye, M.; Ma, N. Ground-Based Evaluation of MODIS Snow Cover Product V6 across China: Implications for the Selection of NDSI Threshold. *Sci. Total Environ.* **2019**, *651*, doi:10.1016/j.scitotenv.2018.10.128.
71. Koskinen, J.T.; Pulliainen, J.T.; Luojus, K.P.; Takala, M. Monitoring of Snow-Cover Properties during the Spring Melting Period in Forested Areas. *IEEE Trans. Geosci. Remote Sens.* **2010**, *48*, doi:10.1109/TGRS.2009.2024755.
72. Solorza, R.; Cogliati, M.; Salcedo, A.P.; Notarnicola, C. Snow Cover Estimation Using L Band SAR Data in the North Patagonian Andes of Argentina. *Rev. la Asoc. Geol. Argentina* **2016**, *73*.
73. Veyssière, G.; Karbou, F.; Morin, S.; Lafaysse, M.; Vionnet, V. Evaluation of Sub-Kilometric Numerical Simulations of C-Band Radar Backscatter over the French Alps against Sentinel-1 Observations. *Remote Sens.* **2019**, *11*, doi:10.3390/rs11010008.
74. Rott, H.; Mätzler, C. Possibilities and Limits of Synthetic Aperture Radar for Snow and Glacier Surveying. *Ann. Glaciol.* **1987**, *9*, doi:10.3189/s0260305500000604.
75. Shi, J.; Dozier, J. Measurements of Snow- and Glacier-Covered Areas with Single- Polarization SAR. *Ann. Glaciol.* **1993**, *17*, doi:10.1017/s0260305500012635.
76. Besic, N.; Vasile, G.; Chanussot, J.; Stankovic, S.; Boldo, D.; D'Urso, G. Wet Snow Backscattering Sensitivity on Density Change for SWE Estimation. In Proceedings of the International Geoscience and Remote Sensing Symposium (IGARSS); 2013.
77. Beltramone, G.; Scavuzzo, M.; German, A.; Ferral, A. Wet Snow Detection in Patagonian Andes with Sentinel-1 SAR Temporal Series Analysis in GEE. In Proceedings of the 2020 IEEE Congreso Bienal de Argentina, ARGENCON 2020 - 2020 IEEE Biennial Congress of Argentina, ARGENCON 2020; 2020.
78. Moravec, G.F.; Danielson, J.A. GRAPHICAL METHOD OF STREAM RUNOFF PREDICTION FROM LANDSAT DERIVED SNOWCOVER DATA FOR WATERSHEDS IN THE UPPER RIO GRANDE BASIN OF COLORADO. *NASA Conf. Publ.* **1979**.

79. Steele, C.; Dialesandro, J.; James, D.; Elias, E.; Rango, A.; Bleiweiss, M. Evaluating MODIS Snow Products for Modelling Snowmelt Runoff: Case Study of the Rio Grande Headwaters. *Int. J. Appl. Earth Obs. Geoinf.* **2017**, *63*, doi:10.1016/j.jag.2017.08.007.
80. Fassnacht, S.R.; Sexstone, G.A.; Kashipazha, A.H.; López-Moreno, J.I.; Jasinski, M.F.; Kampf, S.K.; Von Thaden, B.C. Deriving Snow-Cover Depletion Curves for Different Spatial Scales from Remote Sensing and Snow Telemetry Data. *Hydrol. Process.* **2016**, *30*, doi:10.1002/hyp.10730.
81. Arsenault, K.R.; Houser, P.R. Generating Observation-Based Snow Depletion Curves for Use in Snow Cover Data Assimilation. *Geosci.* **2018**, *8*, doi:10.3390/geosciences8120484.
82. Polo, M.J.; Herrero, J.; Millares, A.; Pimentel, R.; Moñino, A.; Pérez-Palazón, M.J.; Aguilar, C.; Losada, M.A. Snow Dynamics, Hydrology, and Erosion. In *The Landscape of the Sierra Nevada: A Unique Laboratory of Global Processes in Spain*; 2022.
83. Luojus, K.P.; Pulliainen, J.T.; Metsåmäki, S.J.; Hallikainen, M.T. Accuracy Assessment of SAR Data-Based Snow-Covered Area Estimation Method. *IEEE Trans. Geosci. Remote Sens.* **2006**, *44*, doi:10.1109/TGRS.2005.861414.
84. Tsai, Y.L.S.; Dietz, A.; Oppelt, N.; Kuenzer, C. Wet and Dry Snow Detection Using Sentinel-1 SAR Data for Mountainous Areas with a Machine Learning Technique. *Remote Sens.* **2019**, *11*, doi:10.3390/rs11080988.
85. Baghdadi, N.; Gauthier, Y.; Bernier, M. Capability of Multitemporal ERS-1 Data for Wet-Snow Mapping. *Remote Sens. Environ.* **1997**, *60*, doi:10.1016/S0034-4257(96)00180-0.
86. Koskinen, J.T.; Pulliainen, J.T.; Hallikainen, M.T. The Use of Ers-1 Sar Data in Snow Melt Monitoring. *IEEE Trans. Geosci. Remote Sens.* **1997**, *35*, doi:10.1109/36.581975.
87. Rott, H.; Nagler, T. Monitoring Temporal Dynamics of Snowmelt with ERS-1 SAR. In Proceedings of the International Geoscience and Remote Sensing Symposium (IGARSS); 1995; Vol. 3.
88. Baghdadi, N.; Gauthier, Y.; Bernier, M.; Fortin, J.-P. Potential and Limitations of RADARSAT SAR Data for Wet Snow Monitoring. *IEEE Trans. Geosci. Remote Sens.* **2000**, *38*, 316–320, doi:10.1109/36.823925.
89. Li, D.; Lettenmaier, D.P.; Margulis, S.A.; Andreadis, K. The Value of Accurate High-Resolution and Spatially Continuous Snow Information to Streamflow Forecasts. *J. Hydrometeorol.* **2019**, *20*, doi:10.1175/JHM-D-18-0210.1.
90. Arribas, E.C.; Lantarón, J.H.; Porro, C.A.; Gómez, M.J.P. Management and Operation of Small Hydropower Plants through a Climate Service Targeted at End-Users. In Proceedings of the Proceedings - 2019 IEEE International Conference on Environment and Electrical Engineering and 2019 IEEE Industrial and Commercial Power Systems Europe, EEEIC/I and CPS Europe 2019; 2019.
91. Durand, M.; Molotch, N.P.; Margulis, S.A. A Bayesian Approach to Snow Water Equivalent Reconstruction. *J. Geophys. Res. Atmos.* **2008**, *113*, doi:10.1029/2008JD009894.